A Study of Detonation Diffraction and Failure for a Model of Compressible Two-Phase Reactive Flow

D. W. Schwendeman and A. K. Kapila
Department of Mathematical Sciences, Rensselaer Polytechnic Institute,
Troy, New York, 12180

and

W. D. Henshaw
Center for Applied Scientic Computing, Lawrence Livermore National Laboratory,
Livermore, California, 94550

January 6, 2010

Abstract

A two-phase model of heterogeneous explosives, with a reaction rate that is proportional to the gas-phase pressure excess above an ignition threshold, is examined computationally. The numerical approach, a variant of Godunov's method designed to accommodate nonconservative terms in the hyperbolic model, extends previous work of the authors to two-dimensional configurations. The focus is on the behavior of an established detonation as it rounds a 90° corner and undergoes diffraction. The dependence of the post-diffraction conduct on the reaction rate is explored by varying the reaction-rate prefactor and the ignition threshold. The aim is to determine whether the model, as postulated, can capture dead zones, which are pockets of unreacted or partially reacted explosive observed in the vicinity of the corner in diffraction experiments. Results of this study are compared with those of a similar investigation on the one-phase ignition-and-growth model.

1 Introduction

Mathematical modeling of detonation in high-energy condensed-phase explosives presents a variety of challenges, and as such, is a topic of ongoing study. The explosive is typically a non-homogeneous mixture of a myriad of materials, including polycrystalline grains of the energetic constituent of varied distributions and morphology, inert or reactive binders, metallic particulates, additives, and voids. As these components have widely varying constitutive properties, an initiating shock interacting with the microstructure generates a commensurately heterogeneous mechanical response at the granular level, caused by such processes as friction, crystal fracture, plastic deformation, void collapse, shearing, and jetting. This leads to the creation of hot spots, which are small regions significantly hotter than the averaged temperature in the shocked explosive, and hence discrete sites of initiation of chemical reaction. When averaged over a sufficiently large scale, this heterogeneous behavior produces an average heat release rate that is a combination of chemical kinetics at the molecular scale and mechanics at the grain scale. A rational description of the multi-scale behavior would require a thorough characterization of the underlying processes at each relevant scale, followed by homogenization across the scales to produce a model appropriate for the scale of observation. While this goal is being actively pursued, it is not yet a reality. Meanwhile two practical approaches have emerged, both phenomenological, in which balance laws for state variables at the continuum level are supplemented by thermo-mechanical and chemical constitutive expressions. The simpler of these approaches treats the explosive as a homogeneous mixture of two constituents, the reactant and the product, in mechanical and

thermal equilibrium and subject to a single reaction at a rate that attempts to incorporate microstructural effects. A well-studied example of this approach is the ignition-and-growth model originally proposed by Lee and Tarver [1] and later refined by Tarver and colleagues [2, 3, 4, 5]. The second approach recognizes explicitly the porous nature of the explosive, treating it as a mixture of two distinct but coexisting phases and allowing mutual exchange of mass, momentum and energy across the interfacial boundaries. Constitutive expressions for the interfacial exchange accompany the balance laws; they incorporate the micromechanical submodels and their formulation is constrained by thermodynamic principles. A prominent example of this approach is the two-phase model considered by Baer and Nunziato [6].

The success of each model is determined by the fidelity to which it is able to capture, and even predict, experimentally observed phenomena in a variety of experiments. Suitably calibrated, both types of models have performed well in replicating various aspects of planar, one-dimensional experiments; see, for example, Tarver and colleagues cited above for the ignition-and-growth model, and Baer and collaborators [6, 7, 8] for the two-phase model. Nonplanar geometries, however, have been more of a challenge. Consider, in particular, the appearance of dead zones in corner-turning. Experiments have shown that when a well-established detonation diffracts around a sharp corner, it leaves behind a sustained pocket of unreacted material, or a dead zone, in the vicinity of the corner [9, 10, 11]. In earlier studies we have demonstrated that the standard ignition-and-growth model does not admit dead zones for either rigid [12] or compliant [13] confinement. In a later study [14] we considered a modification of the ignition-and-growth model to account for the effect of desensitization by weak shocks, and this enhanced model was shown to be capable of admitting dead zones. An alternate approach to desensitization was proposed in [15]. To our knowledge, no studies on detonation diffraction have been reported for the two-phase model.

Recently we have proposed a new numerical approach for the two-phase equations [16] which is a variant of the Godunov method and includes a rational treatment of the non-conservative nozzling terms of the model. We have employed it to examine in detail the evolution to detonation following a weak planar impact in a one-dimensional configuration [17]. In the present paper we extend this numerical approach to two space dimensions. The equations are discretized on overlapping grids to handle complex flow geometry, and adaptive mesh refinement is used to increase the grid resolution locally following the approach discussed in [18]. The computations are performed in parallel following the method outlined in [19]. The extended computational capability is employed to study detonation diffraction at a corner, and to explore in particular whether dead zones can be captured by the two-phase model without requiring the explicit introduction of a desensitization submodel. The calculations assume rigid confinement, similar to that used in [12] for the ignition-and-growth model.

In a computational study of the two-phase continuum model, a core issue that must be faced at the outset is the selection of the constitutive terms. Previous studies of two-phase models have generally focused on specific explosives or classes of explosives, which in turn has led their authors to particular constitutive choices for the equations of state. However, the choices have been remarkably uniform as far as the rate of energy release is concerned. For example, Baer and Nunziato [6] considered combustion of spherical HMX grains at a rate proportional to the pressure in the gas phase. In the treatment by Baer *et al* [7] of the granular explosive CP, and by Gonthier and Powers [20] of granulated explosives more generally, a similar burn rate was employed, along with a specified ignition-temperature trigger. Baer and Nunziato chose a two-step reactive model in their later study of ball propellants [8], adding a compaction-induced hot-spot combustion reaction dependent upon mixture pressure to the gas-phase pressure-dependent burn rate. In a subsequent effort due to Gonthier and Powers [21] the ignition-temperature switch was replaced by an induction delay driven by an Arrhenius-like source. Chinnayya *et al* [22] accommodated a mixture of materials such as ammonium perchlorate and aluminum particles by including a multi-step kinetic scheme but keeping the pressure dependence of the rate constants. Thus, a common characteristic of the kinetic choices has been the dependence of the rate of reaction on the pressure in the gas phase, motivated by surface regression behavior of condensed explosives. We adopted a similar form, slightly modified to include a minimum pressure threshold for ignition, in our earlier work [17] and have opted to retain it in the present study. The equations of state for the two phases are also the same as in [17], an ideal equation of state with a stiffening term for the solid phase and a virial equation of state for the gas phase. We emphasize that this work is aimed less at the characteristics of a particular explosive than at the generic behavior. The intent is to determine whether a feature observed in nonplanar experiments is admitted by a model which has been

reasonably successful in reproducing observed phenomena in nominally one-dimensional experiments. To carry out this examination, constitutive input and exchange-rate parameters are calibrated to sound speeds, steady detonation speeds, reaction-zone thicknesses, etc., typical of PBX-type explosives. The numerical method itself is general enough and can be used with other sets of parameters, or with other modeling choices and reaction rates.

With the constitutive forms at hand, we have carried out two preliminary studies to determine the appropriate parameter space for exploring the reaction rate. The first study sets the reaction rate to zero and computes piston-driven, planar compaction waves to determine the maximum gas-phase pressure achieved in a steady compaction wave as a function of the piston speed. This information provides estimates of the range in which the gas-phase pressure threshold for ignition must lie. The second study sets the gas-phase pressure threshold for ignition at a value only very slightly above the ambient gas-phase pressure, and examines the post-diffraction gas-phase pressure drop in the resulting detonation to assess what a reasonable ignition threshold must be if the reaction is to undergo any extinction at all subsequent to diffraction. With the relevant range of reaction-rate parameters established in this way, we have selected a set for exploration, for which we first compute the corresponding steady detonation structures and then the response of the detonation to corner turning. The results show that both temporary and sustained dead zones can occur, and that the precise evolution scenario depends upon a delicate balance between the ignition threshold and the reaction-rate prefactor.

The remaining sections of the paper are organized as follows. Section 2 presents the governing equations and the constitutive assumptions. Model parameters typical of practical explosives and reference scales for nondimensionalization are introduced in Section 3. Section 4 presents a brief introduction to the numerical method and includes a grid resolution study carried out to insure accurate resolution of fine features. Results of the numerical investigation appear in Section 5, and conclusions are drawn in Section 6.

2 Governing equations

The governing equations follow those employed in [17] for one-dimensional flow. These equations are similar to those in the two-phase model proposed originally in [6], but some of the modeling choices are slightly different. A full discussion of this issue appears in [23]. When extended to two dimensions, the governing equations of the two-phase model have the form

$$\frac{\partial}{\partial t}\mathbf{u} + \frac{\partial}{\partial x_1}\mathbf{f}_1(\mathbf{u}) + \frac{\partial}{\partial x_2}\mathbf{f}_2(\mathbf{u}) = \mathbf{h}_1(\mathbf{u})\frac{\partial \bar{\alpha}}{\partial x_1} + \mathbf{h}_2(\mathbf{u})\frac{\partial \bar{\alpha}}{\partial x_2} + \mathbf{k}(\mathbf{u}), \tag{1}$$

where the state variable $\mathbf{u}$ and fluxes $\mathbf{f}_i(\mathbf{u})$, $i = 1, 2$ are given by

$$\mathbf{u} = \begin{bmatrix} \bar{\alpha} \\ \bar{\alpha}\bar{\rho} \\ \bar{\alpha}\bar{\rho}\bar{v}_1 \\ \bar{\alpha}\bar{\rho}\bar{v}_2 \\ \bar{\alpha}\bar{\rho}\bar{E} \\ \alpha\rho \\ \alpha\rho v_1 \\ \alpha\rho v_2 \\ \alpha\rho E \end{bmatrix}, \qquad \mathbf{f}_1(\mathbf{u}) = \begin{bmatrix} 0 \\ \bar{\alpha}\bar{\rho}\bar{v}_1 \\ \bar{\alpha}(\bar{\rho}\bar{v}_1^2 + \bar{p}) \\ \bar{\alpha}\bar{\rho}\bar{v}_1\bar{v}_2 \\ \bar{\alpha}\bar{v}_1(\bar{\rho}\bar{E} + \bar{p}) \\ \alpha\rho v_1 \\ \alpha(\rho v_1^2 + p) \\ \alpha\rho v_1 v_2 \\ \alpha v_1(\rho E + p) \end{bmatrix}, \qquad \mathbf{f}_2(\mathbf{u}) = \begin{bmatrix} 0 \\ \bar{\alpha}\bar{\rho}\bar{v}_2 \\ \bar{\alpha}\bar{\rho}\bar{v}_1\bar{v}_2 \\ \bar{\alpha}(\bar{\rho}\bar{v}_2^2 + \bar{p}) \\ \bar{\alpha}\bar{v}_2(\bar{\rho}\bar{E} + \bar{p}) \\ \alpha\rho v_2 \\ \alpha\rho v_1 v_2 \\ \alpha(\rho v_2^2 + p) \\ \alpha v_2(\rho E + p) \end{bmatrix},$$

and the source terms on the right-hand-side are

$$\mathbf{h}_1(\mathbf{u}) = \begin{bmatrix} -\bar{v}_1 \\ 0 \\ p \\ 0 \\ p\bar{v}_1 \\ 0 \\ -p \\ 0 \\ -p\bar{v}_1 \end{bmatrix}, \qquad \mathbf{h}_2(\mathbf{u}) = \begin{bmatrix} -\bar{v}_2 \\ 0 \\ 0 \\ p \\ p\bar{v}_2 \\ 0 \\ 0 \\ -p \\ -p\bar{v}_2 \end{bmatrix}, \qquad \mathbf{k}(\mathbf{u}) = \begin{bmatrix} \mathcal{F} + \mathcal{C}/\bar{\rho} \\ \mathcal{C} \\ \mathcal{M}_1 \\ \mathcal{M}_2 \\ \mathcal{E} - p\mathcal{F} \\ -\mathcal{C} \\ -\mathcal{M}_1 \\ -\mathcal{M}_2 \\ -\mathcal{E} + p\mathcal{F} \end{bmatrix}.$$

Here, α, ρ, (v_1, v_2) and p denote the volume fraction, density, velocity and pressure of the gas phase, respectively, and $\bar{\alpha}$, $\bar{\rho}$, $(\bar{v}_1, \bar{v}_2)$ and $\bar{p}$ denote the analogous quantities of the solid phase. (The bar superscript is used throughout to indicate solid phase quantities.) The total energies are given by

$$E = e + \frac{1}{2}\left(v_1^2 + v_2^2\right), \qquad \bar{E} = \bar{e}_s + \frac{1}{2}\left(\bar{v}_1^2 + \bar{v}_2^2\right),$$

where e is the specific internal energy of the gas and $\bar{e}_s = \bar{e} + \bar{B}(\bar{\alpha}) + \bar{q}$ is the specific internal energy of the solid. The internal energy of the solid is the sum of the internal energy of the pure solid $\bar{e}$, the compaction potential energy $\bar{B}(\bar{\alpha})$ and the heat release $\bar{q}$. The compaction potential accounts for the configuration-dependent energy of the solid (see [23]). Following [17], we take

$$\bar{B}(\bar{\alpha}) = \frac{(p_0 - \bar{p}_0)(2 - \bar{\alpha}_0)^2}{\bar{\alpha}_0 \bar{\rho}_0 \ln(1 - \bar{\alpha}_0)} \ln\left[\left(\frac{2 - \bar{\alpha}_0}{2 - \bar{\alpha}}\right) \frac{(1 - \bar{\alpha})^{(1-\bar{\alpha})/(2-\bar{\alpha})}}{(1 - \bar{\alpha}_0)^{(1-\bar{\alpha}_0)/(2-\bar{\alpha}_0)}}\right],$$

where the zero subscript denotes quantities given by a reference ambient state. (A similar form for $\bar{B}(\bar{\alpha})$ was used in [24].) In addition, following our work in [17], we employ a virial equation of state for the gas phase and a stiffened equation of state for the solid phase so that

$$e(\rho, p) = \frac{p}{(1 - \gamma)\rho(1 + b\rho)}, \qquad \bar{e}(\bar{\rho}, \bar{p}) = \frac{\bar{p} + \bar{\gamma}\bar{\pi}}{(\bar{\gamma} - 1)\bar{\rho}}, \tag{2}$$

where γ and $\bar{\gamma}$ are ratios of specific heats, b is a virial gas coefficient, and $\bar{\pi}$ is a solid stiffening pressure. Finally, the volume fractions satisfy the saturation constraint,

$$\alpha + \bar{\alpha} = 1,$$

which closes the system of equations.

The first equation in (1) describes the compaction dynamics of the two-phase flow, while the remaining equations represent the balance of mass, momentum and energy for each phase. The non-conservative, or nozzling, terms appear on the right hand side of (1) and are proportional to the gradient of the volume fraction, $(\partial\bar{\alpha}/\partial x_1, \partial\bar{\alpha}/\partial x_2)$. These terms model interphase momentum and energy transfer that occurs as a result of an effective change in the cross-sectional area of the virtual stream tube of the gas phase. The last term on the right hand side of (1) gives the exchange of mass, momentum and energy between phases due to compaction, drag, heat transfer, and chemical reaction (see [6, 23]). The rate of compaction is given by

$$\mathcal{F} = -\frac{\alpha\bar{\alpha}}{\mu_c}(p - \bar{p} + \bar{\beta}), \tag{3}$$

where μ_c is the compaction viscosity and $\bar{\beta} = \bar{\alpha}\bar{\rho}\bar{B}'(\bar{\alpha})$ is the configuration pressure. The exchange of mass due to chemical reaction is given by $\mathcal{C} < 0$. The form for $\mathcal{C}$ depends on the assumed reaction kinetics, and we have chosen the a pressure-ignition model following the discussion in [17]. This rate has the form

$$\mathcal{C} = \begin{cases} 0 & \text{if } p < p_{\text{ign}}, \\ -\sigma\bar{\alpha}\bar{\rho}(p - p_{\text{ign}}) & \text{if } p \geq p_{\text{ign}}, \end{cases} \tag{4}$$

where σ is a rate constant and $p_{\rm ign}$ is an ignition pressure. The exchange of momentum is given by

$$\mathcal{M}_i = \mathcal{C}\bar{v}_i + \left(\delta + \frac{1}{2}\mathcal{C}\right)(v_i - \bar{v}_i), \qquad i = 1\,,\ 2\,, \tag{5}$$

where δ is a drag coefficient. The exchange of momentum involves two terms, one proportional to the rate of mass exchange due to chemical reaction and the other proportional to δ. The former contributes to the rate of momentum exchange by taking the velocity to be the average of the phase velocities, while the latter measures drag and involves the difference between the phase velocities. Finally, the exchange of energy is given by

$$\mathcal{E} = \left(\bar{E} + \frac{\beta}{\bar{\rho}}\right)\mathcal{C} + \sum_{i=1}^{2}(\mathcal{M}_i - \mathcal{C}\bar{v}_i)\bar{v}_i + \mathcal{H}(T - \bar{T}), \tag{6}$$

where $\mathcal{H}$ is an interphase heat transfer coefficient, and T and $\bar{T}$ are temperatures of the gas and solid phases, respectively. These temperatures are given by

$$C_v T = \frac{p}{(\gamma - 1)\rho(1 + b\rho)}, \qquad \bar{C}_v \bar{T} = \frac{\bar{p} + \bar{\gamma}\bar{\pi}}{(\bar{\gamma} - 1)\bar{\rho}},$$

where C_v and $\bar{C}_v$ are specific heats at constant volume. The exchange of energy in (6) involves three terms, the first is the rate of energy production due to mass exchange, the second is the rate of working associated with momentum exchange, and the third is energy exchange due to heat transfer.

3 Reference scales and model parameters

For the remainder of the paper, we choose to work with dimensionless quantities. To accomplish this, we first introduce dimensional reference scales following the choices made in [17]. For the numerical calculations presented in Section 5, we consider a representative explosive with an ambient upstream state given by

$$\begin{aligned} &\alpha_0 = .27, \quad &&\rho_0 = 1\ \text{kg/m}^3, \quad &&p_0 = .25225\ \text{MPa}, \quad &&T_0 = 300\ \text{K}, \\ &\bar{\alpha}_0 = .73, \quad &&\bar{\rho}_0 = 1900\ \text{kg/m}^3, \quad &&\bar{p}_0 = 7.6\ \text{MPa}, \quad &&\bar{T}_0 = 300\ \text{K}. \end{aligned}$$

Parameters for the equations of state in (2) are taken to be

$$\gamma = 1.35, \qquad b = 0.001\ \text{m}^3/\text{kg}, \qquad \bar{\gamma} = 5, \qquad \bar{\pi} = 3412.4\ \text{MPa},$$

and values for the heat release and for the specific heats are taken to be

$$\bar{q} = 6.65 \times 10^6\ \text{J/kg}, \qquad C_v = 2400\ \text{J/(kg K)}, \qquad \bar{C}_v = 1500\ \text{J/(kg K)}.$$

From these choices, quantities at the steady CJ state may be computed (see [17]). In particular, the steady CJ detonation velocity is found to be

$$D_{\rm CJ} = 7508.8\ \text{m/s},$$

and the corresponding density, velocity, pressure and temperature at the CJ state are

$$\rho_{\rm CJ} = 1906.2\ \text{kg/m}^3, \qquad v_{\rm CJ} = 2044.3\ \text{m/s}, \qquad p_{\rm CJ} = 21.300\ \text{GPa}, \qquad T_{\rm CJ} = 4577.1\ \text{K}.$$

Reference scales are now constructed from the steady CJ detonation velocity, the pressure at the CJ state, and the choices

$$t_{\rm ref} = 1\ \mu\text{s}, \qquad C_{v,\rm ref} = 2400\ \text{J/(kg K)}. \tag{7}$$

These scales are

$$\begin{aligned} &v_{\rm ref} = D_{\rm CJ} = 7508.8\ \text{m/s}, \quad &&p_{\rm ref} = p_{\rm CJ} = 21.300\ \text{GPa}, \\ &x_{\rm ref} = v_{\rm ref} t_{\rm ref} = 7.5088 \times 10^{-3}\ \text{m}, \quad &&\rho_{\rm ref} = p_{\rm ref}/v_{\rm ref}^2 = 377.78\ \text{kg/m}^3, \\ &T_{\rm ref} = v_{\rm ref}^2/C_{v,\rm ref} = 23492^\circ\ \text{K}, \quad &&E_{\rm ref} = v_{\rm ref}^2 = 5.6381 \times 10^7\ \text{J/kg}. \end{aligned} \tag{8}$$

Param.	Value	Param.	Value
$\bar{\alpha}_0$	0.73	$\bar{\gamma}$	5
$\bar{\rho}_0$	5.0293	$\bar{\pi}$	0.16021
$\bar{p}_0$	3.5682e−4	$\bar{C}_v$	0.625
$\bar{T}_0$	1.2770e−2	$\bar{q}$	0.11795
ρ_0	2.6470e−3	γ	1.35
p_0	1.1843e−5	b	0.37778
T_0	1.2770e−2	C_v	1

Table 1: Dimensionless upstream state and equation of state parameters.

Dimensionless quantities may now be defined in the usual way by dividing each dimensional quantity by its corresponding reference scale given in (7) or (8). The result leaves the governing equations in (1) unchanged, and the corresponding dimensionless upstream state and equation of state parameters are listed in Table 1. In addition, we require dimensionless parameters for the compaction viscosity in (3), the drag coefficient in (5), and the heat transfer coefficient in (6). For the purposes of this paper, we choose nominal values from the range of values considered in [17]. These dimensionless values are

$$\mu_c = 0.05, \qquad \delta = 20.0, \qquad \mathcal{H} = 0.2 \; .$$

The remaining parameters of the two-phase model, σ and $p_{\rm ign}$, are needed for the reaction rate in (4), and these will be chosen later in Section 5 for the particular numerical experiments studied.

4 Numerical method

The numerical method used to solve the governing equations in (1) is a high-resolution Godunov method. The equations are discretized on an overlapping grid consisting of a set of curvilinear component grids as discussed in Section 4.1. The calculations are performed in parallel and employ adaptive mesh refinement (AMR) to locally increase the grid resolution near contacts, shocks and detonations, so that well-resolved solutions are obtained. A Strang-type fractional-step scheme is used to advance the equations in time. One step handles the nonlinear convection portion of the equations with the non-differentiated sources terms set to zero, while the other step considers these source terms alone. Details of our fractional-step scheme are given in Section 4.2. Two test problems are discussed in Section 4.3, and these are used to indicate the convergence behavior of the numerical method.

4.1 Overlapping grid framework

An overlapping grid for a flow domain Ω consists of a set of component grids $\{\mathcal{G}_k\}$, $k = 1, \ldots, \mathcal{N}_g$, that cover Ω and overlap where they meet. Typically the bulk of the domain is covered by Cartesian grids while smooth boundary-fitted grids are used to represent the boundary of the domain. For example, an overlapping grid which describes the flow geometry for the corner-turning calculations discussed in Section 5 is shown in Figure 1. The overlapping grid (on the base level of refinement) consists of three component grids, each defined by a smooth mapping $\mathbf{x} = G_k(\mathbf{r})$ from computational space $\mathbf{r} = (r_1, r_2)$ on the unit square to physical space $\mathbf{x} = (x_1, x_2)$. The grid shown in red on the left is an "inlet" grid where a steady planar detonation wave is specified initially. The blue grid to the right is a Cartesian "background" grid which represents the bulk of the flow domain. Finally, there is a boundary-fitted green grid which describes the (smoothed) corner. The sharp corner is replaced by a smooth one with a radius of the order of the steady reaction-zone thickness in order to remove the geometric singularity there. This smoothing has little effect on the solution away from the corner. (See also the discussion in [12] for example.) The three component grids shown in Figure 1 overlap as shown in the enlarged view of the grid on the right, and bi-linear interpolation is used to communication the state variables of the flow from one component grid to another in the overlap region (see [18] for further details).

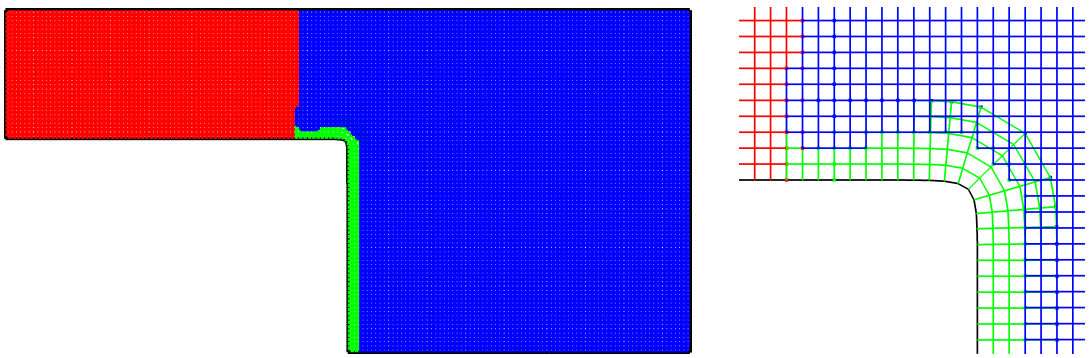

Figure 1: Overlapping grid for the corner-turning flow geometry (left) and enlarged view near the corner (right). The inlet grid is red, the background Cartesian grid is blue, and the boundary-fitted grid is green. The (dimensionless) horizontal and vertical lengths are 8 and 4, respectively. (The resolution of the grid is reduced by a factor of 8 for illustrative purposes.)

Block-structured AMR is employed following the approach described originally in [25]. Refined-grid patches are created and used to cover regions of the flow where the solution changes rapidly while coarser grids are used where the solution is smooth. This allows us to perform calculations at a higher resolution than would be possible had the entire domain been covered by a fine grid. Within the overlapping grid framework each refinement grid is defined as a restriction of the smooth mapping $\mathbf{x} = G_k(\mathbf{r})$ belonging to the coarser parent grid. In this manner the refinement grids retain the smooth description of the boundary. All grids in the overlapping-grid system, including base-level grids and refinement grids, are treated the same within the computational kernels so that implementation of the AMR algorithm is greatly simplified. Further details of our AMR approach for overlapping grids, including the choice for an error estimate and the regridding algorithm, are discussed in [18].

The numerical method is implemented in parallel using a domain-decomposition approach based on our previous work in [19]. The implementation is flexible so that each base grid within the overlapping-grid structure and its associated refinement grids can be independently partitioned over a chosen set of processors. A modified bin-packing algorithm is used to specify the partition for each grid so that the computational work is evenly distributed amongst the processors. All components of the AMR algorithm such as error estimation, regridding, and interpolation are performed in parallel. The corner-turning calculations discussed later in Section 5 were run on a linux cluster with 32 processors.

4.2 Discretization of the governing equations

The discretization of the governing equations in (1) is carried out on each component grid $\mathcal{G}_k$, $k = 1, \ldots, \mathcal{N}_g$, in the overlapping-grid system. As mentioned previously, these grids include both base-level and refinement grids. Each component grid is defined by a mapping $\mathbf{x} = G_k(\mathbf{r})$ from computational space $\mathbf{r} = (r_1, r_2)$ on the unit square to physical space $\mathbf{x} = (x_1, x_2)$. In computation space, the governing equations become

$$\frac{\partial}{\partial t}\mathbf{u} + \frac{1}{J}\left(\frac{\partial}{\partial r_1}\widehat{\mathbf{f}}_1(\mathbf{u}) + \frac{\partial}{\partial r_2}\widehat{\mathbf{f}}_2(\mathbf{u})\right) = \frac{1}{J}\left(\widehat{\mathbf{h}}_1(\mathbf{u})\frac{\partial \bar{\alpha}}{\partial r_1} + \widehat{\mathbf{h}}_2(\mathbf{u})\frac{\partial \bar{\alpha}}{\partial r_2}\right) + \mathbf{k}(\mathbf{u}), \tag{9}$$

where

$$\widehat{\mathbf{f}}_\ell = a_{\ell,1}\mathbf{f}_1(\mathbf{u}) + a_{\ell,2}\mathbf{f}_2(\mathbf{u}), \qquad \widehat{\mathbf{h}}_\ell = a_{\ell,1}\mathbf{h}_1(\mathbf{u}) + a_{\ell,2}\mathbf{h}_2(\mathbf{u}), \qquad \ell = 1, 2,$$

are mapped fluxes and coefficients of the nozzling terms, respectively, and

$$J = \left|\frac{\partial(x_1, x_2)}{\partial(r_1, r_2)}\right|, \qquad a_{\ell,m} = J\left(\frac{\partial r_\ell}{\partial x_m}\right), \qquad \ell = 1, 2, \quad m = 1, 2, \tag{10}$$

are given by the mapping $\mathbf{x} = G_k(\mathbf{r})$.

The numerical method for the mapped equations in (9) follows that described in [16, 17] for the two-phase model in one space dimension. The method employs a second-order, Strang-type, fractional-step scheme of the form

$$\mathbf{U}_{i,j}^{n+1} = \mathcal{S}_k(\Delta t/2)\,\mathcal{S}_h(\Delta t)\,\mathcal{S}_k(\Delta t/2)\,\mathbf{U}_{i,j}^{n},$$

where $\mathbf{U}_{i,j}^{n}$ denotes the cell average of $\mathbf{u}(\mathbf{r},t)$ at a time t_n on a uniform grid $\mathbf{r}_{i,j}$ with mesh spacings $(\Delta r_1, \Delta r_2)$. A global time step Δt is used for all component grids for the step from t_n to t_{n+1}, and its value is chosen to satisfy a CFL stability condition. The operators $\mathcal{S}_h(\tau)$ and $\mathcal{S}_k(\tau)$ represent numerical integrations of the equations

$$\frac{\partial}{\partial t}\mathbf{u} + \frac{1}{J}\left(\frac{\partial}{\partial r_1}\widehat{\mathbf{f}}_1(\mathbf{u}) + \frac{\partial}{\partial r_2}\widehat{\mathbf{f}}_2(\mathbf{u})\right) = \frac{1}{J}\left(\widehat{\mathbf{h}}_1(\mathbf{u})\frac{\partial \bar{\alpha}}{\partial r_1} + \widehat{\mathbf{h}}_2(\mathbf{u})\frac{\partial \bar{\alpha}}{\partial r_2}\right), \tag{11}$$

and

$$\frac{\partial}{\partial t}\mathbf{u} = \mathbf{k}(\mathbf{u}), \tag{12}$$

respectively, over a time interval τ. The integration of (11) uses a second-order, slope-limited Godunov method, which is modified to handle the non-conservative nozzling terms following the approach described originally in [16] and extended in [17] to handle a virial equation of state for the gas phase. The integration of (12) uses a second-order, adaptive Runge-Kutta method as described in [17]. Since the fractional-step scheme and the integration of (12) have been described already for one-dimensional flow, we focus here on the integration of (11) for two-dimensional flow which is new.

The hydro step, $\widehat{\mathbf{U}}_{i,j} = \mathcal{S}_h(\Delta t)\mathbf{U}_{i,j}$, uses a finite-volume discretization of (11) of the form

$$\begin{aligned}\widehat{\mathbf{U}}_{i,j} = \mathbf{U}_{i,j} &- \frac{\Delta t}{\Delta r_1 J_{i,j}}\left[\mathbf{F}^{L}_{1,i+1/2,j} - \mathbf{F}^{R}_{1,i-1/2,j}\right] \\ &- \frac{\Delta t}{\Delta r_2 J_{i,j}}\left[\mathbf{F}^{L}_{2,i,j+1/2} - \mathbf{F}^{R}_{2,i,j-1/2}\right] + \frac{\Delta t}{\Delta r_1 J_{i,j}}\widetilde{\mathbf{H}}_{1,i,j} + \frac{\Delta t}{\Delta r_2 J_{i,j}}\widetilde{\mathbf{H}}_{2,i,j},\end{aligned} \tag{13}$$

where $\mathbf{F}^{L,R}_{1,i\pm1/2,j}$ and $\mathbf{F}^{L,R}_{2,i,j\pm1/2}$ are numerical fluxes (including leading order contributions of the nozzling terms), $J_{i,j}$ is the Jacobian of the mapping evaluated on the grid, and $\widetilde{\mathbf{H}}_{\ell,i,j}$, $\ell = 1,2$ are second-order corrections of the discretization of the nozzling terms. The calculation of the fluxes and the second-order corrections of the nozzling terms is performed in a two-step manner. The first step involves computing first-order, slope-limited values at the cell faces, $\mathbf{r}_{i\pm1/2,j}$ and $\mathbf{r}_{i,j\pm1/2}$, at $t = t_n + \Delta t/2$, and the second step uses these values as left and right states for a Riemann problem. The solution of the Riemann problem is then used to compute $\mathbf{F}^{L,R}_{1,i\pm1/2,j}$, $\mathbf{F}^{L,R}_{2,i,j\pm1/2}$ and $\widetilde{\mathbf{H}}_{\ell,i,j}$ in (13). Further details can be found in [16, 17].

Let us focus, for example, on the calculation of $\mathbf{F}^{L,R}_{1,i+1/2,j}$, the numerical fluxes at the cell face $\mathbf{r}_{i+1/2,j}$. In order to compute slope-limited values at the cell face, we consider the quasi-linear form of (11) given by

$$\frac{\partial}{\partial t}\mathbf{w} + A_1(\mathbf{w})\frac{\partial}{\partial r_1}\mathbf{w} + A_2(\mathbf{w})\frac{\partial}{\partial r_2}\mathbf{w} = 0, \tag{14}$$

where $\mathbf{w} = [\bar{\alpha}, \bar{\rho}, \bar{v}_1, \bar{v}_2, \bar{p}, \rho, v_1, v_2, p]^T$ is a vector of primitive variables. The coefficient matrices in (14) are given by

$$A_\ell(\mathbf{w}) = \frac{1}{J}\begin{bmatrix}
\bar{u}_\ell & 0 & 0 & 0 & 0 & 0 & 0 & 0 & 0 \\
0 & \bar{u}_\ell & a_{\ell,1}\bar{\rho} & a_{\ell,2}\bar{\rho} & 0 & 0 & 0 & 0 & 0 \\
-a_{\ell,1}\Delta p/(\bar{\alpha}\bar{\rho}) & 0 & \bar{u}_\ell & 0 & a_{\ell,1}/\bar{\rho} & 0 & 0 & 0 & 0 \\
-a_{\ell,2}\Delta p/(\bar{\alpha}\bar{\rho}) & 0 & 0 & \bar{u}_\ell & a_{\ell,2}/\bar{\rho} & 0 & 0 & 0 & 0 \\
0 & 0 & a_{\ell,1}\bar{\rho}\bar{c}^2 & a_{\ell,2}\bar{\rho}\bar{c}^2 & \bar{u}_\ell & 0 & 0 & 0 & 0 \\
-\rho\Delta u_\ell/\alpha & 0 & 0 & 0 & 0 & u_\ell & a_{\ell,1}\rho & a_{\ell,2}\rho & 0 \\
0 & 0 & 0 & 0 & 0 & 0 & u_\ell & 0 & a_{\ell,1}/\rho \\
0 & 0 & 0 & 0 & 0 & 0 & 0 & u_\ell & a_{\ell,2}/\rho \\
-\rho c^2\Delta u_\ell/\alpha & 0 & 0 & 0 & 0 & 0 & a_{\ell,1}\rho c^2 & a_{\ell,2}\rho c^2 & u_\ell
\end{bmatrix},$$

where the Jacobian J and metrics $a_{\ell,m}$ of the mapping are given in (10), and

$$\bar{u}_\ell = a_{\ell,1}\bar{v}_1 + a_{\ell,2}\bar{v}_2, \qquad u_\ell = a_{\ell,1}v_1 + a_{\ell,2}v_2, \qquad \Delta u_\ell = u_\ell - \bar{u}_\ell, \qquad \Delta p = p - \bar{p},$$

for $\ell = 1, 2$. The sound speeds, $\bar{c}$ and c, for the solid and gas phases, respectively, are given by

$$\bar{c}^2 = \frac{\bar{\gamma}(\bar{p} + \bar{\pi})}{\bar{\rho}}, \qquad c^2 = \frac{\gamma p}{\rho}\left[1 + b\rho - \frac{b^2\rho^2}{\gamma(1+b\rho)}\right].$$

A first-order approximation for $\mathbf{w}$ at $\mathbf{r}_{i+1/2,j}$ is given by

$$\begin{aligned} \mathbf{w}^+_{i+1/2,j} &= \mathbf{w}^n_{i,j} + \frac{\Delta r_1}{2}\left(\frac{\partial \mathbf{w}}{\partial r_1}\right)^n_{i,j} + \frac{\Delta t}{2}\left(\frac{\partial \mathbf{w}}{\partial t}\right)^n_{i,j} \\ &= \mathbf{w}^n_{i,j} + \frac{1}{2}\left(I - \frac{\Delta t}{\Delta r_1}A^n_{1,i,j}\right)\delta_1 \mathbf{w}^n_{i,j} - \frac{\Delta t}{2\Delta r_2}A^n_{2,i,j}\delta_2 \mathbf{w}^n_{i,j}, \end{aligned} \tag{15}$$

where $A^n_{\ell,i,j} = A_\ell(\mathbf{w}^n_{i,j})$, $\ell = 1, 2$, and $\delta_\ell \mathbf{w}^n_{i,j}$ is a discrete approximation for $(\partial_{r_\ell}\mathbf{w})^n_{i,j}\Delta r_\ell$. Slope-limiting is performed in characteristic variables. Let Λ_ℓ be a diagonal matrix of eigenvalues of A_ℓ, and let R_ℓ be the corresponding matrix of (right) eigenvectors so that $A_\ell R_\ell = R_\ell \Lambda_\ell$. Characteristic variables are then defined by $\mathbf{z}_\ell = R_\ell^{-1}\mathbf{w}$, $\ell = 1, 2$. In terms of these characteristic variables, (15) becomes

$$\mathbf{w}^+_{i,j} = \mathbf{w}^n_{i,j} + \frac{1}{2}R^n_{1,i,j}\left(I - \frac{\Delta t}{\Delta r_1}\max\{\Lambda^n_{1,i,j}, 0\}\right)\delta_1 \mathbf{z}^n_{1,i,j} - \frac{\Delta t}{2\Delta r_2}R^n_{2,i,j}\Lambda^n_{2,i,j}\delta_2 \mathbf{z}^n_{2,i,j}, \tag{16}$$

where

$$\delta_1 \mathbf{z}^n_{1,i,j} = \text{minmod}\left((R_{1,i,j})^{-1}(\mathbf{w}^n_{i+1,j} - \mathbf{w}^n_{i,j}),\, (R_{1,i,j})^{-1}(\mathbf{w}^n_{i,j} - \mathbf{w}^n_{i-1,j})\right),$$

and

$$\delta_2 \mathbf{z}^n_{2,i,j} = \text{minmod}\left((R_{2,i,j})^{-1}(\mathbf{w}^n_{i,j+1} - \mathbf{w}^n_{i,j}),\, (R_{2,i,j})^{-1}(\mathbf{w}^n_{i,j} - \mathbf{w}^n_{i,j-1})\right).$$

Here, the maximum and minimum-modulus functions are performed component-wise. Similar steps give

$$\mathbf{w}^-_{i+1/2,j} = \mathbf{w}^n_{i+1,j} - \frac{1}{2}R^n_{1,i+1,j}\left(I + \frac{\Delta t}{\Delta r_1}\min\{\Lambda^n_{1,i+1,j}, 0\}\right)\delta_1 \mathbf{z}^n_{1,i+1,j} - \frac{\Delta t}{2\Delta r_2}R^n_{2,i+1,j}\Lambda^n_{2,i+1,j}\delta_2 \mathbf{z}^n_{2,i+1,j}, \tag{17}$$

which is a slope-limited approximation at the cell face $\mathbf{r}_{i+1/2,j}$ from the cell at $\mathbf{r}_{i+1,j}$.

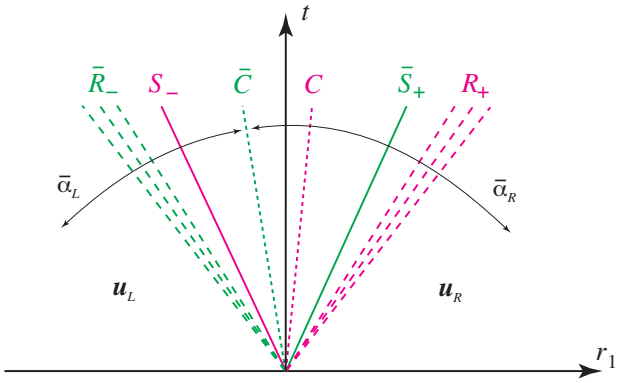

Figure 2: A representative solution of the one-dimensional Riemann problem in the r_1-direction consisting of shocks, rarefactions and contact discontinuities indicated by the symbols S, R and C, respectively.

The numerical fluxes $\mathbf{F}^{L,R}_{1,i+1/2,j}$ are obtained from the solution of the one-dimensional Riemann problem

$$\frac{\partial}{\partial t}\mathbf{u} + \frac{1}{J}\left(\frac{\partial}{\partial r_1}\widehat{\mathbf{f}}_1(\mathbf{u}) - \widehat{\mathbf{h}}_1(\mathbf{u})\frac{\partial \bar{\alpha}}{\partial r_1}\right) = 0, \qquad \text{with} \quad \mathbf{u}(r_1, 0) = \begin{cases} \mathbf{u}_L & \text{if } r_1 < 0, \\ \mathbf{u}_R & \text{if } r_1 > 0. \end{cases} \tag{18}$$

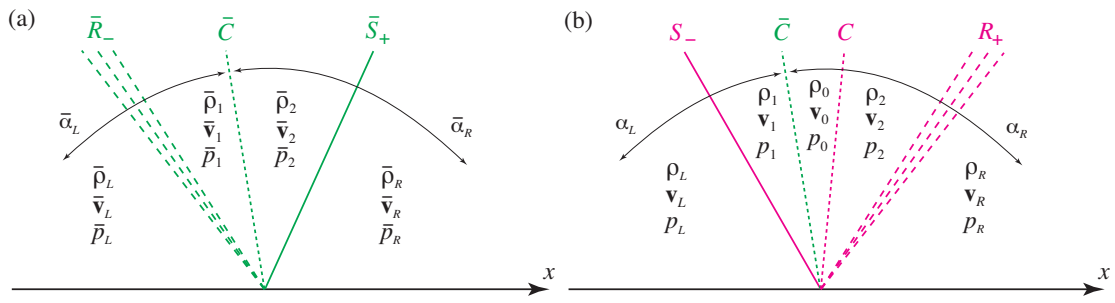

Figure 3: Intermediate states of the (a) solid and (b) gas phases for a subsonic solid contact.

Here, $\mathbf{u}_L$ and $\mathbf{u}_R$ are conserved variables corresponding to the primitive states from (16) and (17), respectively. A representative solution of (18) is shown in Figure 2. The solution consists of shocks, rarefactions and a contact discontinuity in the gas phase all of which at constant $\bar{\alpha}$ (either $\bar{\alpha}_L$ or $\bar{\alpha}_R$ as indicated in the figure). There is also a contact discontinuity in the solid phase where $\bar{\alpha}$ jumps and the phases couple. The solution shown is a so-called "subsonic" case in which the solid contact lies between the acoustics fields of the gas. This is relevant for the case of high drag between the phases as is studied here. Figure 3 shows the intermediates states of the solution for each phase separately, and the central task of a solution procedure is to obtain these states given $\mathbf{u}_L$ and $\mathbf{u}_R$. Our solution approach follows that discussed in [16, 17] with minor modifications made to handle the Jacobian and metric terms (which are evaluated at $\mathbf{r}_{i+1/2,j}$ and held constant) and the passive component of velocity in the direction tangential to the face $r_1 = \text{constant}$ for each phase. In Figure 3, for example, the components of the solid velocity $\bar{\mathbf{v}}$ normal and tangent to $r_1 = \text{constant}$ are given by

$$\bar{v}_n = \frac{(a_{1,1}, a_{1,2})}{\sqrt{a_{1,1}^2 + a_{1,2}^2}} \cdot \bar{\mathbf{v}}, \qquad \bar{v}_t = \frac{(-a_{1,2}, a_{1,1})}{\sqrt{a_{1,1}^2 + a_{1,2}^2}} \cdot \bar{\mathbf{v}},$$

respectively, with similar expressions for the normal and tangential components of the gas velocity $\mathbf{v}$. The solution procedure for the intermediate states $(\bar{\rho}_m, \bar{v}_{n,m}, \bar{p}_m)$, $m = 1, 2$, of the solid and the intermediate states $(\rho_m, v_{n,m}, p_m)$, $m = 0, 1, 2$, of the gas follows that described in our earlier papers, and typically an approximate solution is used to reduce computational cost. Once these states are known, the numerical fluxes $\mathbf{F}^{L,R}_{1,i+1/2,j}$ are found by including the tangential component of the velocity from either the left or right states depending on whether the contacts for the solid and gas lie to the left or right of the line $r_1 = 0$. For example, the flux would be computed using the tangential component of the solid velocity from the right state and the tangential component of the gas velocity from the left state according the solution shown in Figure 3.

The numerical fluxes $\mathbf{F}^{L,R}_{2,i,j+1/2}$ are obtained in a similar manner from the solution of a corresponding one-dimensional Riemann problem in the r_2-direction with suitable left and right values found from first-order, slope-limited approximations. It is noted that the (L, R) superscripts indicate that there are two numerical fluxes computed at each face. As mentioned earlier, these quantities combine an approximation of the conservative flux and a leading order discretization of the nozzling terms which is non-conservative so that the flux to the cell on the left may be different than that to the cell on the right (see [16] for the full details). Finally, with the solution of the Riemann problem in hand, the second-order corrections $\widetilde{\mathbf{H}}_{\ell,i,j}$, $\ell = 1, 2$, are computed following the formulas given in [16], again with minor modifications to account for the Jacobian and metric terms, and the two components of the velocity.

4.3 Grid convergence

There are two problems central to the numerical study discussed in Section 5. The first is the initiation of a one-dimensional detonation and its evolution to a steady wave, and the second is the diffraction of a

steady detonation at a 90° corner. In this section we perform a grid resolution study of two representative examples of these problems in order to check the accuracy of the numerical method.

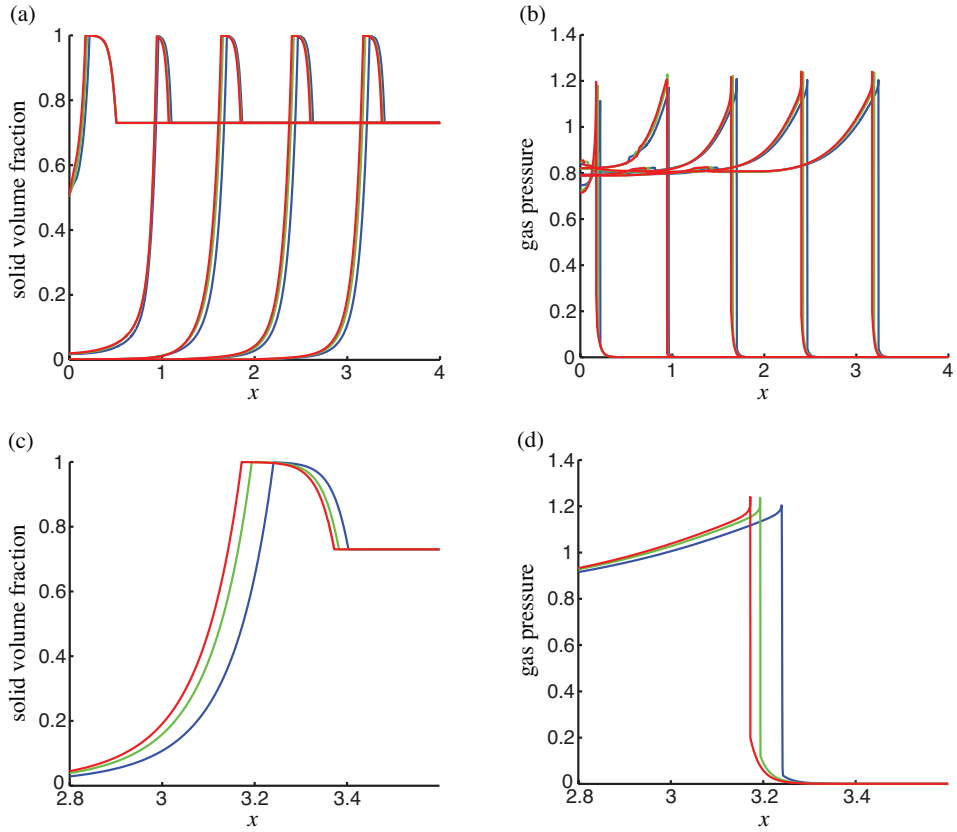

Figure 4: Evolution to detonation for $\sigma = 10$ and $p_{\text{ign}} = 0.45$ at times $t = 1, 2, \ldots, 5$: (a) solid volume fraction and (b) gas pressure. Effective grid spacing $h_{\text{eff}} = 1/1600$ (blue curves), $1/6400$ (green curves) and $1/25600$ (red curves). Plots (c) and (d) show zoomed views at $t = 5$.

For the first example we consider evolution to detonation in one space dimension. The initial state of the reactive material, and the parameters for the equations of state and relaxation terms, are those given in Section 3. The dimensionless prefactor and ignition threshold for the reaction rate in (4) are taken to be $\sigma = 10$ and $p_{\text{ign}} = 0.45$, respectively, which are representative of the values considered in Section 5 (see Table 2). The detonation is initiated by a high-speed piston impact of $v_{\text{piston}} = 0.2131$ which corresponds to 1600 m/s. In order to judge convergence, we compare solutions computed using three grids with effective grid spacings $h_{\text{eff}} = 1/1600$, $1/6400$ and $1/25600$. Figure 4 shows the behavior of the solid volume fraction $\bar{\alpha}$ and the gas pressure p from these three solutions. The plots in Figure 4(a) and (b) show the evolution to detonation at (dimensionless) times $t = 1, 2, \ldots, 5$, and these indicate that the three solutions are in good qualitative agreement. There is some quantitative difference in the solutions, primarily seen as a very small shift in position generated early in the evolution due to the difference in the time when the reaction first occurs at the back of the leading compaction wave (see the plot of $\bar{\alpha}$ at $t = 1$). The time of first reaction occurs when the gas pressure exceeds the threshold p_{ign} and this is sensitive to the grid resolution. The plots in Figure 4(c) and (d) show enlarged views of $\bar{\alpha}$ and p at $t = 5$, and these give a clearer indication of the convergence behavior of the developed detonation wave. The curves of $\bar{\alpha}$ are very similar to one another apart from a shift in position which becomes smaller as h_{eff} gets smaller. The curves of p show this shift as well, and we also note that the peak pressure is nearly the same for the solutions at the two finest resolutions, again indicating convergence as the grid is refined.

As a second example we consider the diffraction of a steady detonation at a 90° corner. For this example

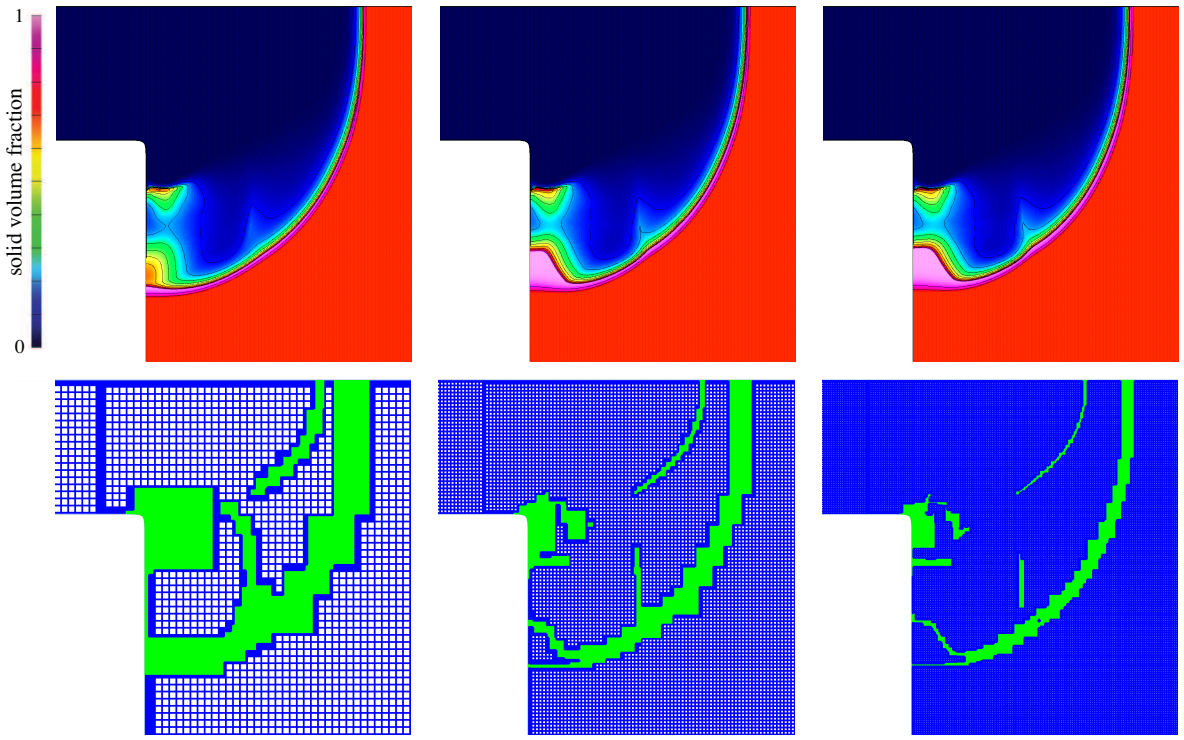

Figure 5: Detonation diffraction for $\sigma = 25$ and $p_{\text{ign}} = 0.53$ at time $t = 3.5$. The top row shows shaded contours of $\bar{\alpha}$ and the bottom row shows the corresponding AMR grids (which are coarsened for illustrative purposes). The left plots use a grid with $h_{\text{eff}} = 1/400$, the middle plots use $h_{\text{eff}} = 1/800$ and the right plots use $h_{\text{eff}} = 1/1600$.

we take $\sigma = 25$ and $p_{\text{ign}} = 0.53$ for the reaction rate and compute the steady, one-dimensional detonation wave on a fine grid with $h_{\text{eff}} = 1/6400$. This solution is then used as the initial state for two-dimensional calculations using the flow geometry shown previously in Figure 1. The leading edge of the steady detonation is positioned initially in the inlet portion of the grid so that it travels to the right and meets the corner at $t = 1$. Our main interest is in the behavior of the diffracted wave for $t > 1$. In order to judge convergence for this problem, we compute solutions on overlapping grids with $h_{\text{eff}} = 1/400$, $1/800$ and $1/1600$. Due to the higher cost of computing two-dimensional solutions, the grid resolutions for this problem are coarser than those considered for the one-dimensional problem. Figure 5 shows shaded contours of the solid volume fraction and corresponding AMR grids for these solutions at $t = 3.5$. The diffracted detonation wave consists of a leading compaction layer (shown as a thin layer of pink where $\bar{\alpha} \approx 1$) which is followed by a reaction zone where $\bar{\alpha}$ decreases to zero. Near the centerline, the detonation remains thin and is not affected strongly by the diffraction at this time. Near the inner (vertical) wall, the detonation has been weakened by the diffraction which results in a thickening of the leading compaction layer. The plots of $\bar{\alpha}$ at the two finer resolutions show good qualitative agreement of this behavior whereas the plot at the coarsest resolution does not. For this coarse-grid solution, the error is large enough to change the behavior of the reaction zone behind the leading compaction layer.

A more quantitative view of the behavior of the solutions may be seen in Figure 6. Here, we show the behavior of $\bar{\alpha}$ and p along the inner wall for the three grid resolutions at times $t = 1, 2, 3, 4$. The curves of the solution for the two finest resolutions (shown in red and green) are in very good agreement. As expected, the curves of the solution at the coarsest resolution (shown in blue) are in poor agreement. All further calculations of detonation diffraction are performed at the finest resolution $h_{\text{eff}} = 1/1600$, the plots shown here provide strong evidence that these solutions are well resolved.

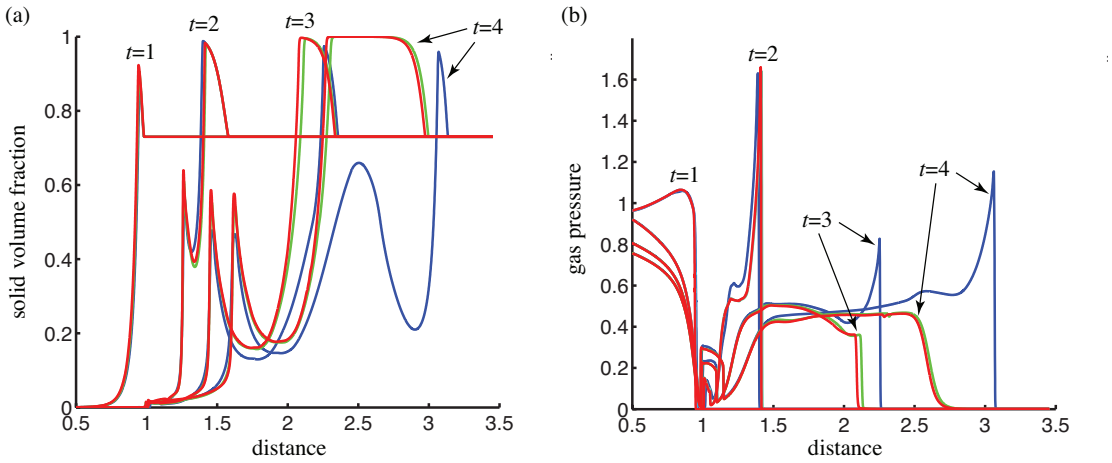

Figure 6: Detonation diffraction for $\sigma = 25$ and $p_{\text{ign}} = 0.53$ at times $t = 1, 2, 3, 4$. Behavior of (a) solid volume fraction and (b) gas pressure along the inner wall. Effective grid spacing $h_{\text{eff}} = 1/400$ (blue curves), $1/800$ (green curves) and $1/1600$ (red curves).

5 Numerical results

In this study the primary intent is to explore the influence of the reaction rate $\mathcal{C}$ given in (4) on the post-diffraction behavior of the detonation. Effects of varying σ, to which the reaction rate is directly proportional, and p_{ign}, which sets the pressure threshold at ignition, are examined. (The remaining parameters of the two-phase model as well as the ambient state of the explosive were given in Section 3.) Computations were carried out over a wide range of parameters but the present discussion is confined to the four cases listed in Table 2.

Case	σ	p_{ign}
I	10	0.45
II	10	0.48
III	25	0.48
IV	25	0.53

Table 2: Reaction pre-factor σ and ignition threshold p_{ign} for Cases I, II, III and IV.

The values of the reaction-rate prefactor in Table 2 are of the same order as those employed in our original study of the evolution of piston-initiated planar detonations [17]. However, the values of p_{ign} are substantially higher than those considered earlier, and this requires some explanation. A low value of p_{ign} has two consequences. First, it allows the detonation to be initiated by rather slow piston speeds, of the order of 100 m/s in the earlier study. Second, it does not allow the possibility of reaction extinction subsequent to corner turning as the gas-phase pressure in the post-diffraction state does not fall below the very low initiation threshold. That, in turn, implies that the reaction-rate model can not admit dead zones at low values of p_{ign}. Since a primary motivation of the present study is to explore whether dead zones are feasible within the framework of the simple reaction rate model that has been adopted, higher values of the ignition threshold need to be considered. Such values, in turn, require a higher piston speed to initiate a detonation wave. Figure 7 shows the relationship between the impact speed of the piston and the maximum gas-phase pressure generated in a compaction wave in the absence of reaction. For a given piston speed the corresponding gas-phase pressure must exceed the ignition threshold for the reaction to begin. For our numerical calculations of the cases listed in Table 2, a piston speed of 1600 m/s is used as this speed is sufficient to overcome the ignition threshold for all four cases.

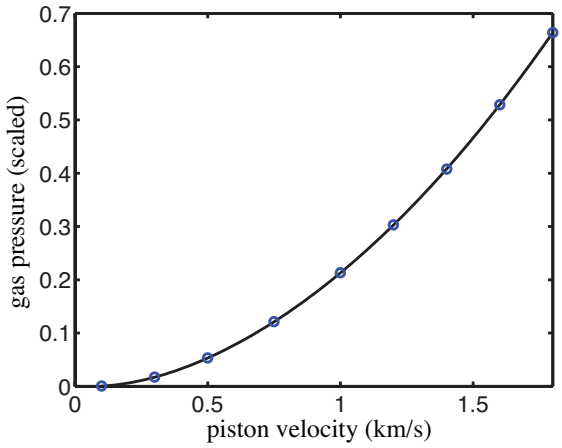

Figure 7: Maximum value of the gas-phase pressure in a reactionless compaction wave as a function of the impact speed provided by the piston

5.1 One-dimensional steady detonation structure

The corner-turning study assumes that a planar, steady detonation has been established in the narrow section of the test configuration upstream of the corner. A brief description of the structure of this detonation is given below, for two cases representative of the four identified in Table 2 and which are to be investigated in the diffraction study that follows in the next section.

Figure 8 displays the structure for the cases $\sigma = 10$ and $p_{\rm ign} = 0.45$ (Case I) and $\sigma = 25$ and $p_{\rm ign} = 0.48$ (Case III). Profiles of the solid volume fraction $\bar{\alpha}$, the solid-phase pressure $\bar{p}$ and the gas-phase pressure p are plotted for both cases. Rates of compaction, reaction and drag given by (3), (4) and $\delta(u-\bar{u})$, respectively, are also plotted. For the lower value of σ shown in Figure 8(a), the structure is led by a shock in the solid phase, followed by a compaction zone in which the solid-phase pressure behind the shock falls and the gas-phase pressure rises very slowly from its ambient value, while the solid volume fraction grows to a near-unity maximum. The compaction zone terminates at the shock in the gas phase as shown in the plot of the compaction rate. The jump in gas pressure across the gas-phase shock switches on the chemical reaction behind it, and as the solid reactant is consumed the pressures fall through the reaction zone, staying in near-equilibrium. The sharp peak in the drag at the start of the reaction zone indicates a very thin layer of velocity disequilibrium, which is caused by the sudden exchange of mass from the solid to the gas phase there. The gas generated by the chemical reaction is essentially unable to penetrate the fully compacted solid ahead of it. The length of the steady detonation structure, defined here as the distance from the leading edge of the compaction layer to the point where $\bar{\alpha} = 0.1$, is found to be 0.413. We note that the case $\sigma = 10$ and $p_{\rm ign} = 0.48$ displays a similar behavior, and both steady structures are similar to the one-dimensional compaction-led structures discussed in [17].

Figure 8(b) shows the steady-state detonation structure for the case $\sigma = 25$ and $p_{\rm ign} = 0.48$. The higher reaction rate corresponding to the larger value of the prefactor leads to a thinner detonation structure, whose thickness is determined to be 0.127. The structure is again led by a solid shock followed by a compaction region, but the peak in the solid volume fraction is now considerably below unity. As a result the gas generated by the reaction, now occurring at a much faster rate, is able to penetrate into the compacted solid to a significant depth in this case. This has two consequences; first, the rise in the gas phase pressure occurs no longer as a jump across a shock but is spread across the penetration depth, and second, the more moderate rate of increase in the gas pressure creates a second, and weaker, compaction zone. These features are also seen clearly in the compaction and drag profiles; the former has a two-tier structure and the latter now displays not a sharp peak but a broad region of velocity disequilibrium. The case $\sigma = 25$ and $p_{\rm ign} = 0.53$ displays a similar behavior.

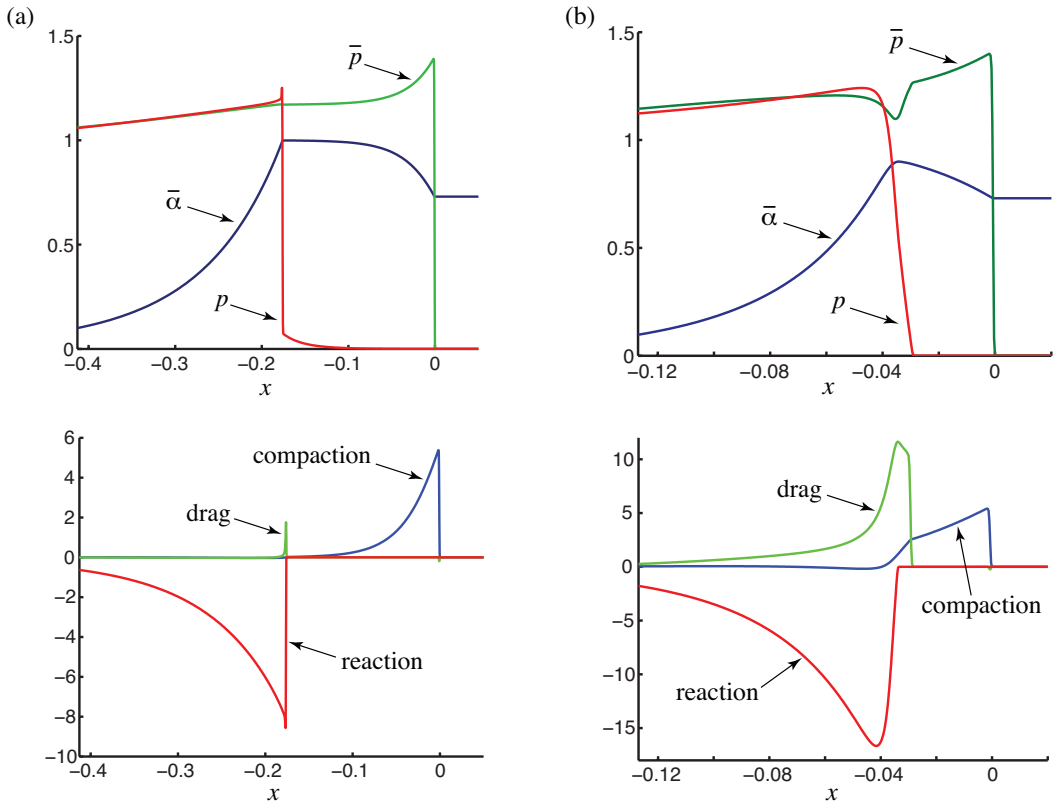

Figure 8: Steady detonation structure for (a) $\sigma = 10$ and $p_{\rm ign} = 0.45$, and (b) $\sigma = 25$ and $p_{\rm ign} = 0.48$. Top frames give profiles of solid volume fraction $\bar{\alpha}$, solid-phase pressure $\bar{p}$ and gas-phase pressure p, and bottom frames give rates of compaction, drag and reaction. The distance x is measured relative the leading edge of the detonation structure for each case. (The reaction rate is scaled by a factor of 5 for illustration purposes.)

It is interesting to note that while the steady detonations for $\sigma = 25$ are both compaction led, the two-zone compaction layer found in these structures was not observed in any of the compaction-led structures in our earlier paper [17]. The reason for this is due primarily to the much larger values of $p_{\rm ign}$ used in the present calculations. For very small values of $p_{\rm ign}$, such as the ones used in [17], a second compaction zone is not needed to raise the gas-phase presure above the ignition threshold. For this case, larger values of the reaction prefactor, σ, result in an evolutionary process in which the shock in the gas phase driven by reaction pushes through the one-zone compaction layer leading to a steady reaction-led detonation (see [17]). For the high values of $p_{\rm ign}$ used here, a very large value of σ would be required to produce a similar evolutionary process. Thus, the steady detonation structure shown in Figure 8(b) is new. It is compaction led, but has a two-zone compaction layer which is observed for higher values of $p_{\rm ign}$.

5.2 Two-dimensional detonation diffraction

We now present the results of diffraction as the steady, planar detonation rounds a 90° corner. The geometry consists of a narrow channel giving way abruptly to a wider channel, as shown in Figure 1. The confining walls are taken to be rigid and the steady detonation is assumed to propagate through the narrow segment prior to rounding the corner. Inlet boundary conditions correspond to flow behind the steady wave, and no-reflection boundary conditions are applied at the outlet. At time $t = 0$ the planar detonation is located in the narrow part of the channel one length unit upstream of the corner, and is propagating steadily towards the corner. The expansion is first sensed by the detonation at time approximately $t = 1$ upon arrival at the

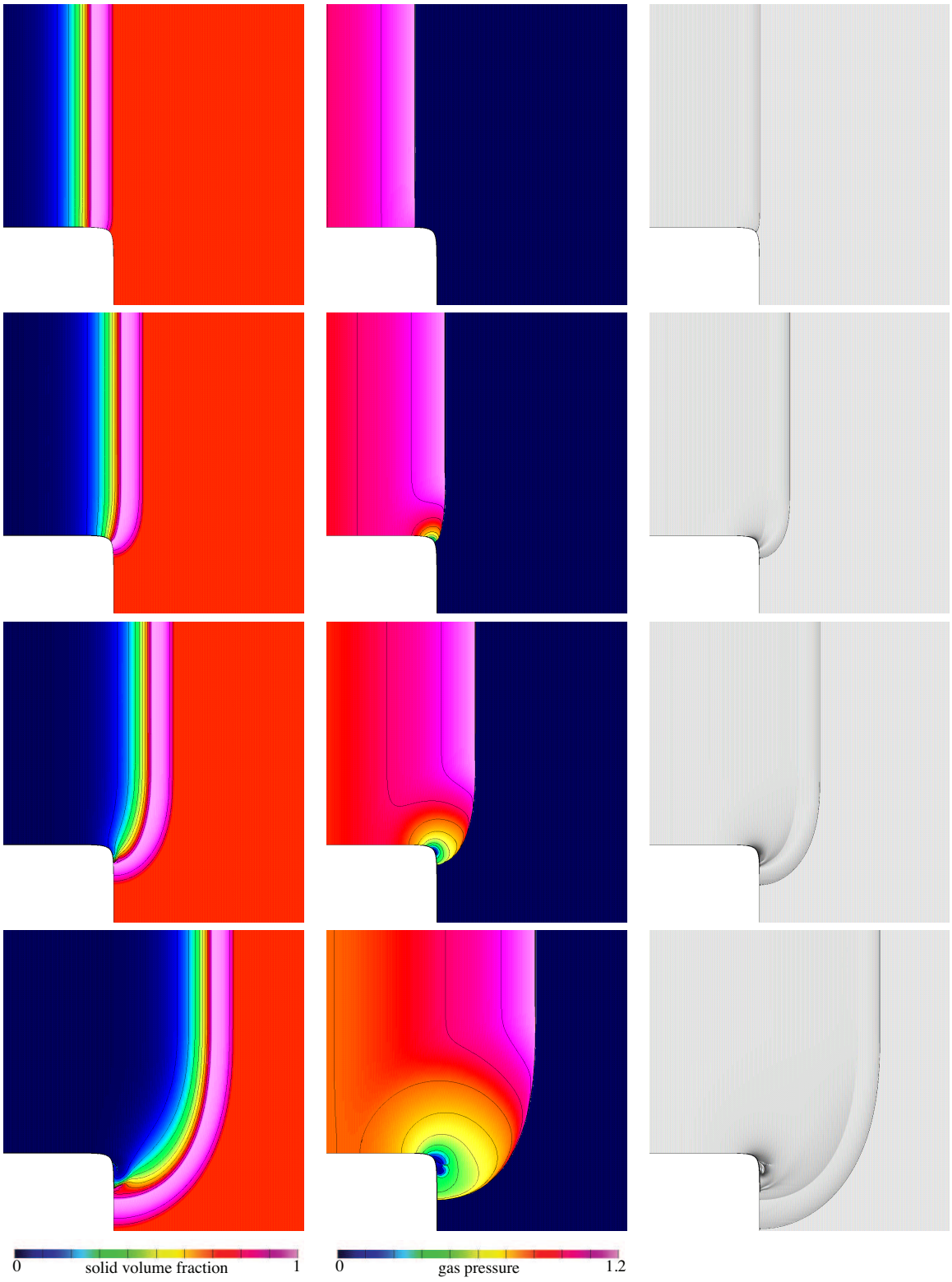

Figure 9: Case I ($\sigma = 10$, $p_{\text{ign}} = 0.45$): Shaded contours of solid volume fraction $\bar{\alpha}$ (left), gas pressure p (middle) and numerically generated schlieren (right) at times $t = 0$ (first row), $t = 1.2$ (second row), $t = 1.4$ (third row) and $t = 1.8$ (fourth row).

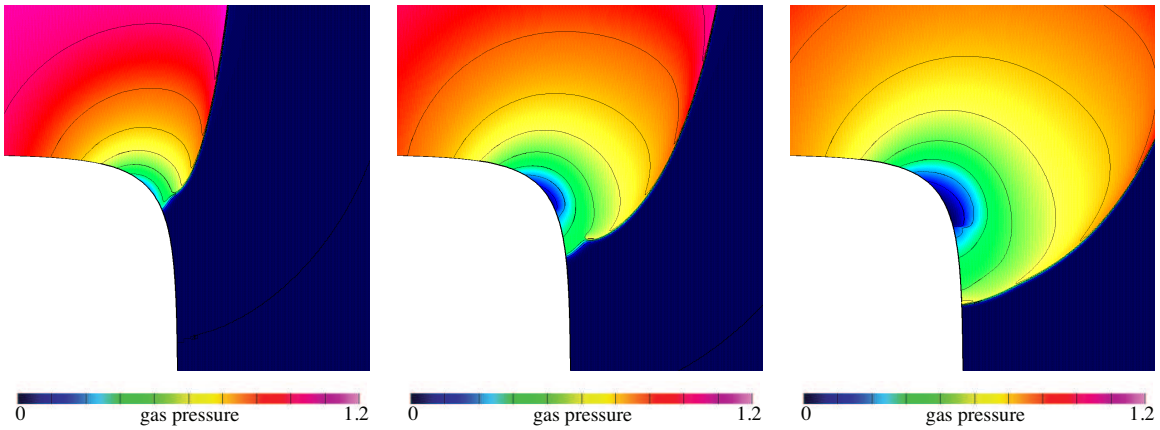

Figure 10: Case I ($\sigma = 10$, $p_{\text{ign}} = 0.45$): Enlarged view of gas pressure p at times $t = 1.2$ (left), $t = 1.3$ (middle) and $t = 1.4$ (right).

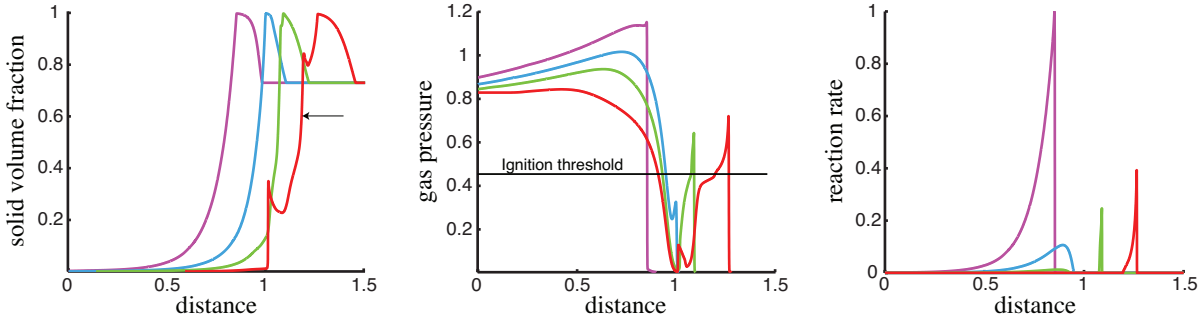

Figure 11: Case I ($\sigma = 10$, $p_{\text{ign}} = 0.45$): Profiles of solid volume fraction (left), gas pressure (middle) and reaction rate (right) along the wall at times $t = 1.0$, 1.2 , 1.4 and 1.8 . The arrow in the solid volume fraction plots points to the sharp interface between partially reacted but frozen region and the reaction zone at time $t = 1.8$.

corner.

Certain general observations can be made before embarking on a detailed description of each of the four cases selected for investigation. As mentioned above, upstream of the corner the wave has a steady, planar structure consisting of a lead shock in the solid phase, followed in turn by a compaction zone, a shock in the gas phase and a reaction zone. Diffraction at the corner reduces the strength of the wave and lends it curvature. This reduction is most pronounced at the corner and along the wall downstream of the corner, and spreads into the interior of the channel away from the corner in a roughly circular region of increasing radius. Reduction in the strength of the solid shock lowers the compaction rate behind it, whereas reduction in the strength of the gas shock lowers the reaction rate behind it. If the reduced pressure at the gas shock were to drop below the ignition threshold, the reaction immediately behind the gas shock would be extinguished. For the parameter choices we have made such extinction does occur in all cases, starting at the wall and extending some distance away from it, while farther away from the wall the reaction continues behind the gas shock albeit at a reduced rate in the region of reduced gas-shock pressure. Thus a point of transition, or kink, is established on the gas shock. Between the wall and this transition point the pressure at the gas shock, already below the ignition threshold, continues to drop. Beyond the transition point away from the wall the gas shock is stronger, with support provided by the reaction behind it. As time evolves the transition point is pushed towards the wall and upon reaching it, raises the gas pressure there to a level above the ignition threshold, thereby reviving the reaction at the wall in a thin layer immediately behind

the gas shock. It is the extent of this revival that determines the fate of the detonation after it has turned the corner.

The four cases listed in Table 2 are now described individually.

5.2.1 Case I ($\sigma = 10$, $p_{\mathbf{ign}} = 0.45$)

The early time results, from $t = 1$ to $t = 1.8$, are shown in Figure 9. A set of three frames is displayed at each time level, corresponding to shaded contours of solid volume fraction, gas pressure and density gradients (highlighting shocks and contact lines), the latter in a numerically generated schlieren plot based on the mixture density $\rho_{\text{mix}} = \alpha\rho + \bar{\alpha}\bar{\rho}$. As the detonation wave rounds the corner it weakens, first in the vicinity of the corner and then in an expanding region centered at the corner, as outlined above. At $t = 1.2$ there emerges a narrow region near the corner in which the gas pressure behind the gas shock has dropped below the ignition threshold $p_{\text{ign}} = 0.45$ and consequently, the reaction there has ceased to occur. Upon close examination of the gas pressure contours at this time (see Figure 10), the aforementioned kink in the gas shock can be seen, above which the pressure behind the gas shock is high enough to keep the reaction from extinction. At time $t = 1.4$ the kink is seen to have reached the wall and disappeared, and at $t = 1.8$ the gas pressure at the wall is found to have returned to levels above the ignition threshold.

Additional insight into the behavior at the wall can be gleaned by examining the profiles of solid volume fraction, gas pressure and reaction rate at the wall, shown in Figure 11. In this figure (and all subsequent wall-plot figures) the ordinate is the distance along the wall, with 1 being the approximate location of the corner, and the (scaled) reaction rate is given by $-\mathcal{C}/\max|\mathcal{C}|$, where the maximum is taken over the times plotted. We note that at $t = 1.2$ the pressure at the gas shock, and in a zone some distance behind it, has fallen to a level below the ignition threshold $p_{\text{ign}} = 0.45$, thereby freezing the reaction in this zone. The reaction does continue to occur behind the frozen zone, to be sure, but at a substantially reduced level. The profiles at subsequent times show the pressure at the gas shock to have suddenly risen to values above the ignition threshold due to the arrival of the kink, thereby reviving the reaction immediately behind the shock. However, this revival is confined to a narrow layer adjacent to the shock, behind which there continues to develop an expanding region of low gas pressure and extinguished reaction. At $t = 1.8$ a sharp interface has appeared in the solid volume fraction profile (shown by arrow), separating the reaction zone adjacent to the gas shock from the layer behind it in which the reaction is frozen. The decline and then the revival of the reaction rate are also on display in the reaction-rate profiles.

The late time results are shown in the shaded contour plots in Figure 12 from $t = 2.0$ to 4.5. As the front advances along the wall the compaction zone, confined to the region between the solid and gas shocks, appears to maintain a nearly constant thickness, a feature that is best seen in the schlieren plots. Behind the gas shock the gas pressure declines, thereby limiting the reaction to a narrow zone behind the gas -phase shock, the zone being thinnest at the wall and becoming thicker away from it. The pocket of low gas pressure and frozen reaction lies behind the reaction zone, hugging the wall and growing in size, and maintaining within it a level of solid volume fraction close to that in the ambient, unreacted explosive.

Supplemental information is provided by the plots of Figure 13, which display profiles of solid volume fraction, gas pressure and reaction rate along the wall. A quasisteady structure with only a partial consumption of reactant emerges, consisting of a compaction zone followed by a narrow reaction layer and a broader region of frozen reaction. The wave gradually gains strength, as exhibited by higher pressures at the gas shock and taller reaction-rate peaks. By the last time level shown a significant increase in the width of the reaction zone has occurred, evident in all three plots but especially in the dip in the solid volume fraction profile within the pocket of hitherto frozen reaction. In brief, diffraction has generated a growing region of partially reacted explosive, in a state of frozen reaction, near the wall. Even though the lead wave is gaining strength, given the proximity of the wavehead to the lower boundary of the configuration there is insufficient room available for the structure to undergo further changes of significance before exiting the domain.

5.2.2 Case II ($\sigma = 10$, $p_{\mathbf{ign}} = 0.48$)

The early time results for this case are very similar to those for Case I above. This is confirmed by the nearly-identical shaded contour plots for the two cases, each at time $t = 1.8$, displayed in Figure 14. There

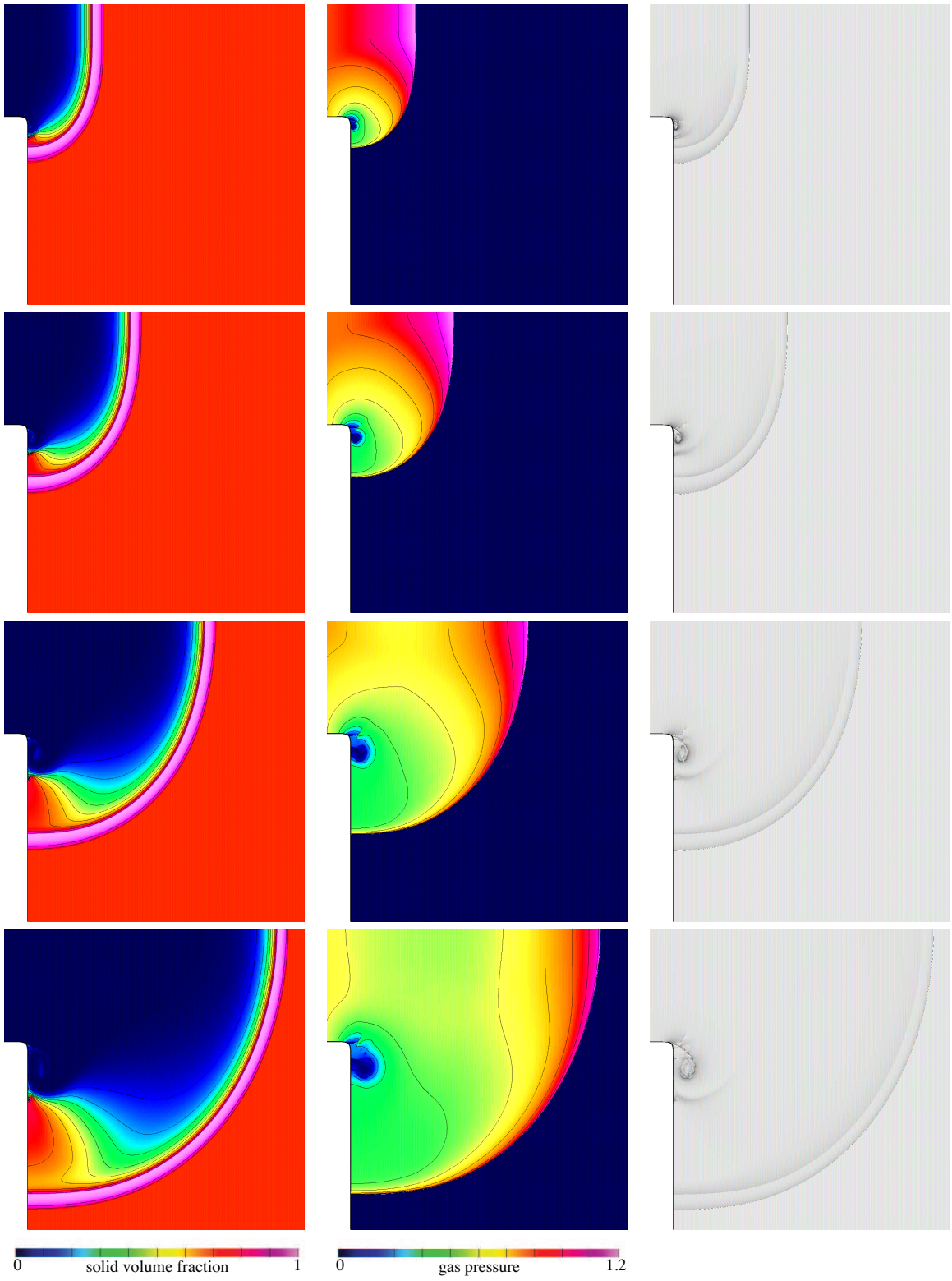

Figure 12: Case I ($\sigma = 10$, $p_{\text{ign}} = 0.45$): Shaded contours of solid volume fraction $\bar{\alpha}$ (left), gas pressure p (middle) and numerically generated schlieren (right) at times $t = 2.0$ (first row), $t = 2.5$ (second row), $t = 3.5$ (third row) and $t = 4.5$ (fourth row).

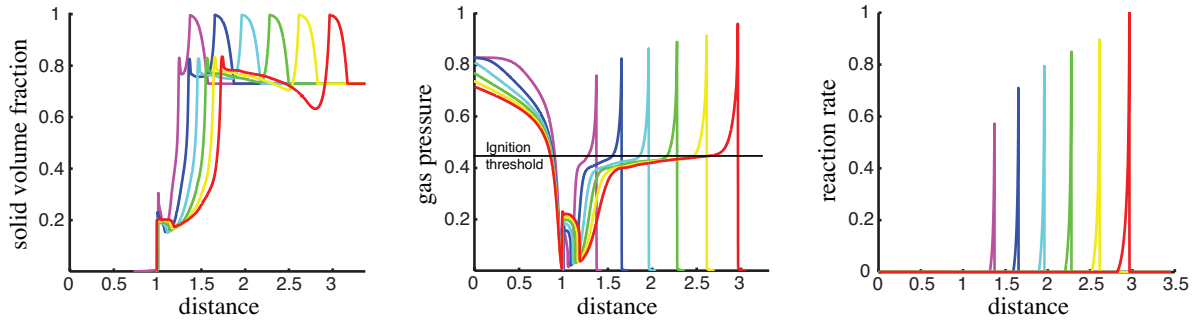

Figure 13: Case I ($\sigma = 10$, $p_{\rm ign} = 0.45$): Profiles of solid volume fraction (left), gas pressure (middle) and the reaction rate (right) along the wall at times $t = 2.0, 2.5, \ldots, 4.5$.

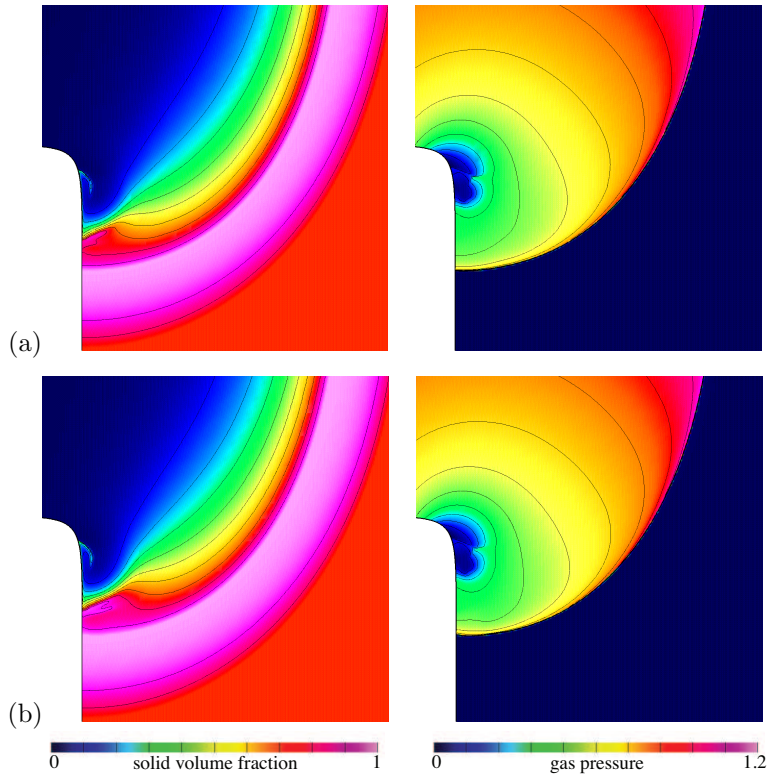

Figure 14: Shaded contours of solid volume fraction $\bar{\alpha}$ (left) and gas pressure p (right) in the vicinity of the corner at time $t = 1.8$ for (a) Case I ($\sigma = 10$, $p_{\rm ign} = 0.45$) and (b) Case II ($\sigma = 10$, $p_{\rm ign} = 0.48$).

are subtle differences between the two cases, however, which will cause evolution for Case II to depart significantly at later times from that for Case I. These differences can be seen in the wall plots for solid volume fraction and gas pressure shown in Figure 15, again for $t = 1.8$. From the solid volume fraction profiles we observe that the waveheads corresponding to the lead compaction waves are essentially at the same location for the two cases. The two compaction zone profiles are also coincident except in the rear, indicating that the compaction zone is thicker for Case II. The gas-phase pressure profiles show that the gas-phase shock for Case II lags behind that for Case I, again confirming the disparity between the widths of the two compaction zones. At the same time the higher ignition threshold for Case II makes the corresponding reaction zone thinner, and this difference in the widths of the reaction zone will play an important role as

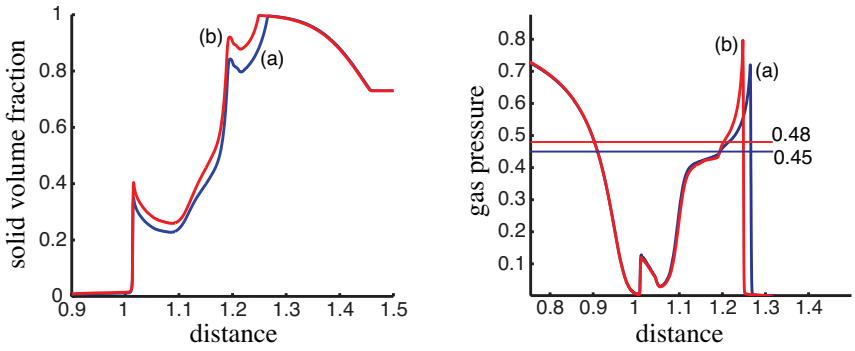

Figure 15: Profiles of solid volume fraction (left) and gas pressure (right) along the wall at time $t = 1.8$ for (a) Case I ($\sigma = 10$, $p_{\rm ign} = 0.45$) and (b) Case II ($\sigma = 10$, $p_{\rm ign} = 0.48$).

the system evolves. Returning to the solid volume fraction profiles again, we note that in the reaction zone at the rear of the compaction zone the reactant consumption for Case II is already much less than that for Case I.

The late time results are shown in the shaded contour plots in Figure 16 from $t = 2.0$ to 4.5 . Again, as in Case I, the compaction zone thickness in the diffracted wave is essentially steady, but now noticeably broader than that in the undiffracted part of the wave close to the channel axis. The compaction zone terminates at the gas shock, behind which the gas pressure in the diffracted wave is low and a growing pocket of frozen reaction develops. Unlike Case I, there is no sign of revival of reaction in this pocket, and it can truly be termed a dead zone.

The wall plots of Figure 17 confirm these features, and show more clearly the quasisteadiness of the structure. Rapid decline of gas pressure in the thin reaction zone is followed by a broadening plateau in which the gas pressure is uniform and below the ignition threshold. The level of compaction in this plateau is also uniform at a level significantly above the ambient but below that in the leading compaction zone, indicating a partially reacted dead zone. It is instructive to compare these wall plots with those in Figure 13; the comparison shows that a small change in the ignition threshold has led to a substantial difference in the eventual outcomes of Cases I and II.

5.2.3 Case III ($\sigma = 25$, $p_{\rm ign} = 0.48$)

It may be argued that a logical choice for Case III at the higher value of σ would just be the Case-I value of the ignition threshold, $p_{\rm ign} = 0.45$. However, since Case I represents a marginal situation in which the diffracted wave contains a partially-reacted near-wall region wherein the reaction is frozen but shows signs of revival, it is clear that increasing the reaction rate would simply make the wave stronger and cause the revival to occur sooner. In order to retain the tension between a stronger rate and a higher threshold, we have elected to present results for $p_{\rm ign} = 0.48$. Thus Case III can be thought to be the counterpart of Case II, and it would be interesting to see if the appearance of the dead zone in Case II is mitigated by the stronger rate due to the higher value of σ .

Shaded contours for early times, from $t = 1.0$ to 1.8 , are shown in Figure 18. The contours of solid volume fraction, at $t = 1$ for example, show that the stronger rate of reaction adopted here generates zones of lead compaction and reaction which are thinner than those in Case II. As before the reaction weakens upon corner turning due to the lowering of the gas pressure, but now the reduced rate of consumption of the compacted reactant allows the compaction zone to become stronger and broader, as seen in both the solid volume fraction and the schlieren diagrams at $t = 1.6$. Away from the corner the gas shock remains strong, and the kink in the gas shock profile (more a hook than a kink in this case) is now visible very prominently at time $t = 1.6$ in all three plots. At time $t = 1.7$ the kink has reached the wall and raised the gas pressure there. The reflected disturbances can be discerned, again in all three plots, at $t = 1.8$.

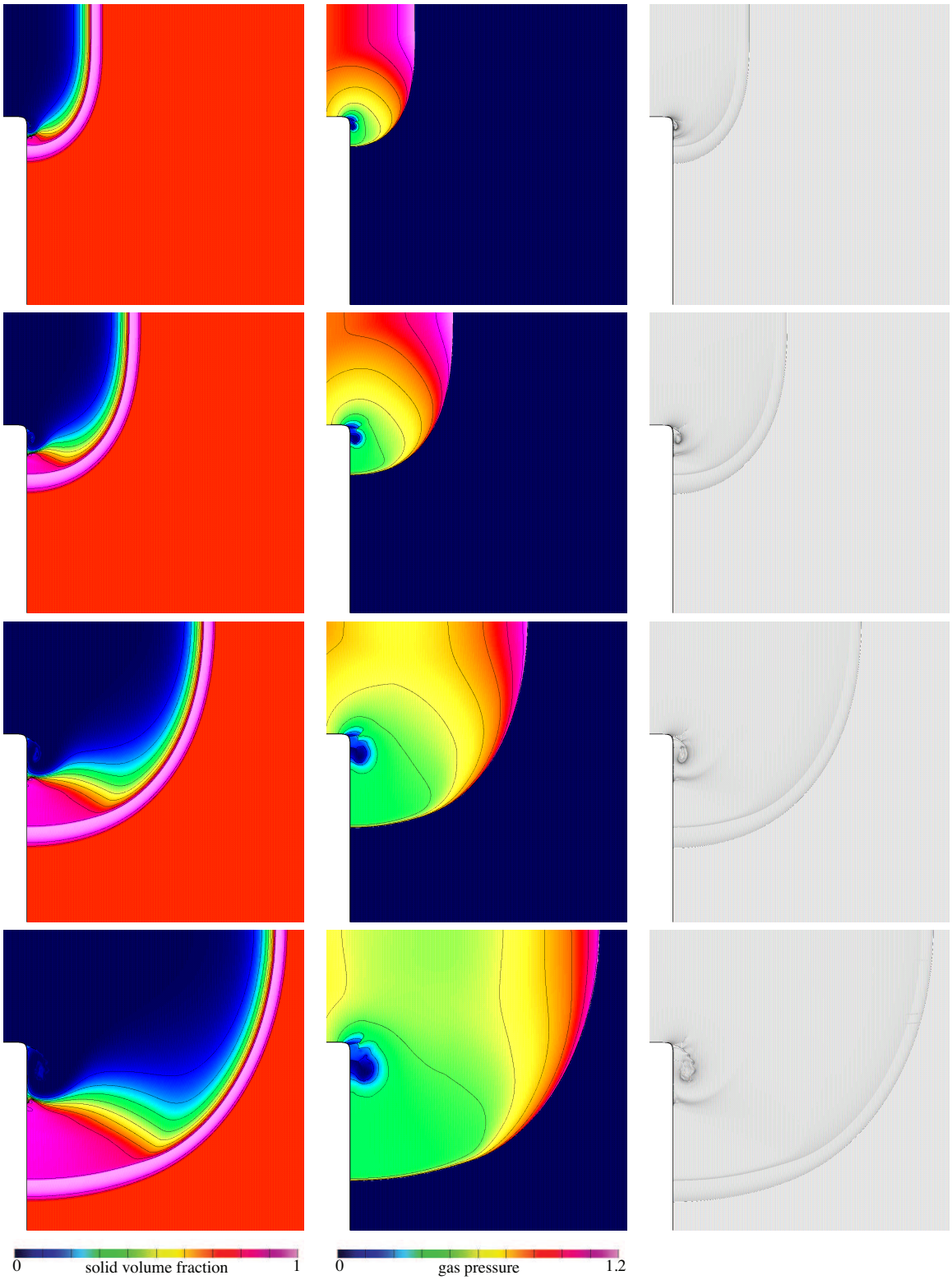

Figure 16: Case II ($\sigma = 10$, $p_{\text{ign}} = 0.48$): Shaded contours of solid volume fraction $\bar{\alpha}$ (left), gas pressure p (middle) and numerically generated schlieren (right) at times $t = 2.0$ (first row), $t = 2.5$ (second row), $t = 3.5$ (third row) and $t = 4.5$ (fourth row).

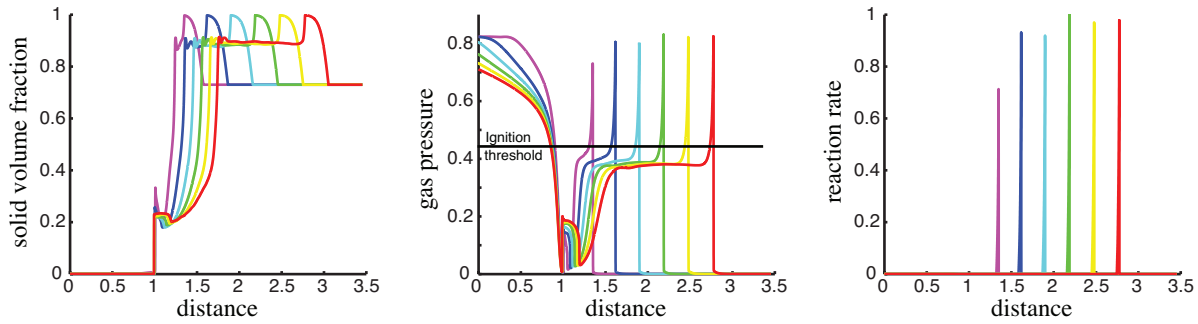

Figure 17: Case II ($\sigma = 10$, $p_{\rm ign} = 0.48$): Profiles of solid volume fraction (left), gas pressure (middle) and the reaction rate (right) along the wall at times $t = 2.0, 2.5, \ldots, 4.5$.

Profiles of solid volume fraction, gas pressure and reaction rate at the wall at early times are plotted in Figure 19. The solid volume profile at $t = 1.0$, just prior to the wave reaching the corner, confirms that although the detonation is compaction-led, the lead compaction zone is thin and in it the solid volume fraction has a peak well below that corresponding to full compaction. At $t = 1.2$ the situation is quite different; the gas pressure at the gas shock has dropped sufficiently to have caused the reaction to cease everywhere, and the loss of reaction has broadened and strengthened the lead compaction zone. At $t = 1.4$ and $t = 1.6$ the reaction remains extinguished and consequently the compaction zone continues to become wider and stronger still. At $t = 1.7$ the gas-pressure peak and hence the reaction rate have undergone a sudden rebirth, the result of lateral reinforcement provided by the slamming of the kink in the gas pressure profile against the wall. At $t = 1.8$ the gas pressure at the wall has acquired a broader profile and although the pressure at the peak is lower it remains well above the ignition threshold, and a similar behavior is evident in the reaction-rate profile as well. At the same time the increased consumption of the compacted reactant has returned the compaction zone to a weaker and narrower profile.

The late time results are shown in the shaded contour plots in Figure 20 from $t = 2.0$ to 4.0 . They show a gradual spreading of the influence of the corner, and a quasisteady evolution of the structure in this region. This structure is led by a thin compaction zone followed by a comparably thin reaction zone in which consumption of the reactant is nearly complete. What distinguishes this structure from that in the pre-diffraction phase is that gas pressure behind the reaction zone is now much lower. These features are confirmed in the wall plots of solid volume fraction, gas pressure and reaction rate shown in Figure 21. The wall plots also confirm the quasisteady evolution of the wave.

5.2.4 Case IV ($\sigma = 25$, $p_{\rm ign} = 0.53$)

We retain the prefactor value at 25 , but increase the ignition threshold to 0.53 . Shaded contours for early times, from $t = 1.0$ to $t = 1.9$, are shown in Figure 22. The situation is similar to that seen in the early-time evolution for Case III, except that the hydrodynamic features are now more striking. The higher value of the ignition threshold causes the reaction, occurring strongly at $t = 1$, to be fully extinguished near the corner as the wave goes around it. The resulting structure, consisting of a thicker compaction zone and lower gas pressures in the near-corner region is evident in the three panels at time $t = 1.4$. In the near-wall region the gas shock separates the fully reacted material from the unreacted but compacted reactant. Away from the wall the gas shock is now hooked, and the hook, clearly visible at $t = 1.4$ in all three plots, has strengthened by time $t = 1.7$ to an extent stronger than that seen in Case III. As the hook advances towards the wall, it raises the gas-phase pressure at the gas shock and revives the reaction behind it. The associated lateral disturbance of high gas pressure approaches the wall, with which it collides at $t = 1.9$.

The loss of reaction upon diffraction is clearly seen in the wall plots of Figure 23, as is the resulting strengthening and widening of the lead compaction zone. The reaction is not revived until $t = 1.9$, when the gas pressure is raised above the ignition threshold by the arrival of the lateral disturbance.

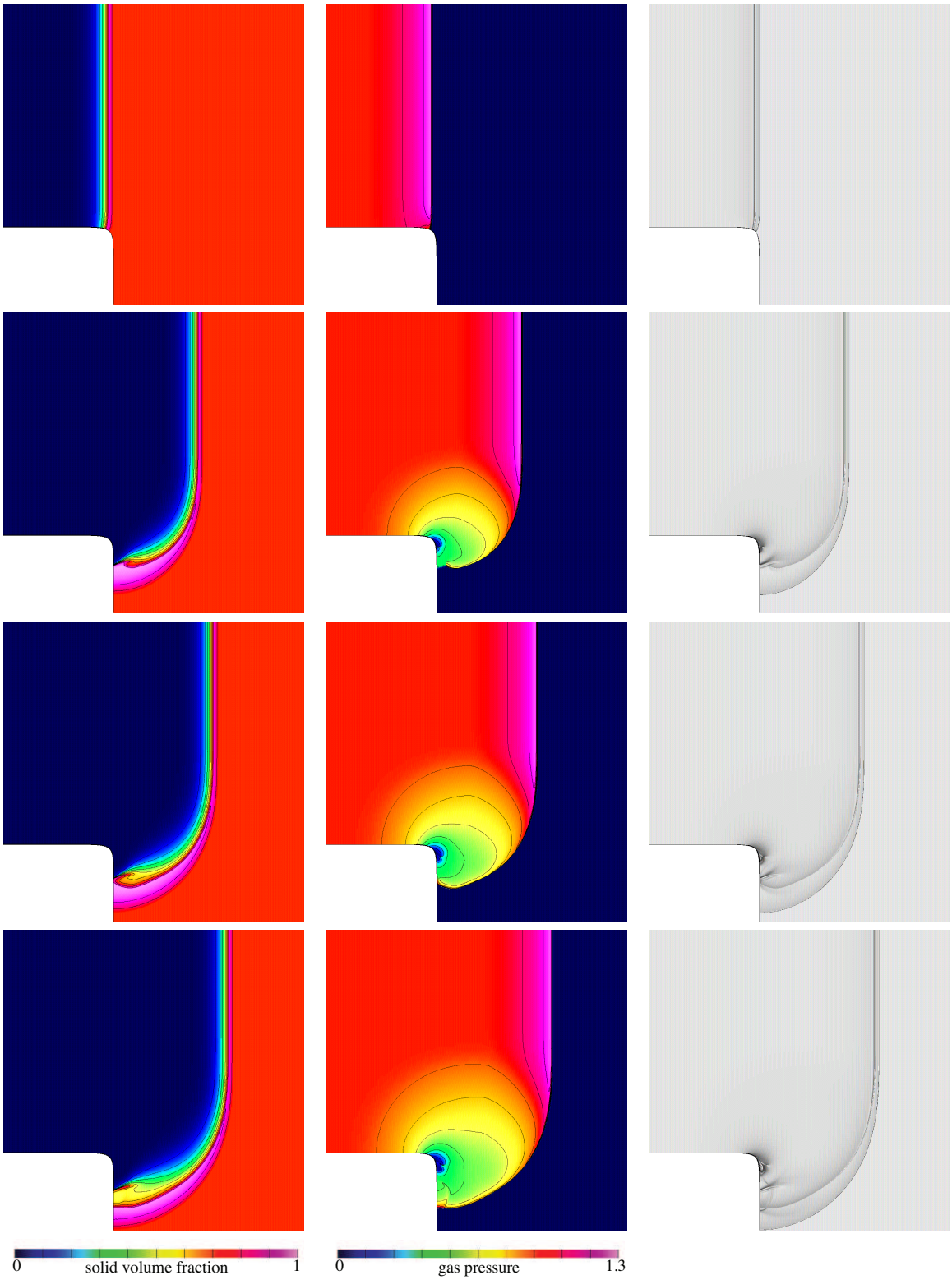

Figure 18: Case III ($\sigma = 25$, $p_{\text{ign}} = 0.48$): Shaded contours of solid volume fraction $\bar{\alpha}$ (left), gas pressure p (middle) and numerically generated schlieren (right) at times $t = 1.0$ (first row), $t = 1.6$ (second row), $t = 1.7$ (third row) and $t = 1.8$ (fourth row).

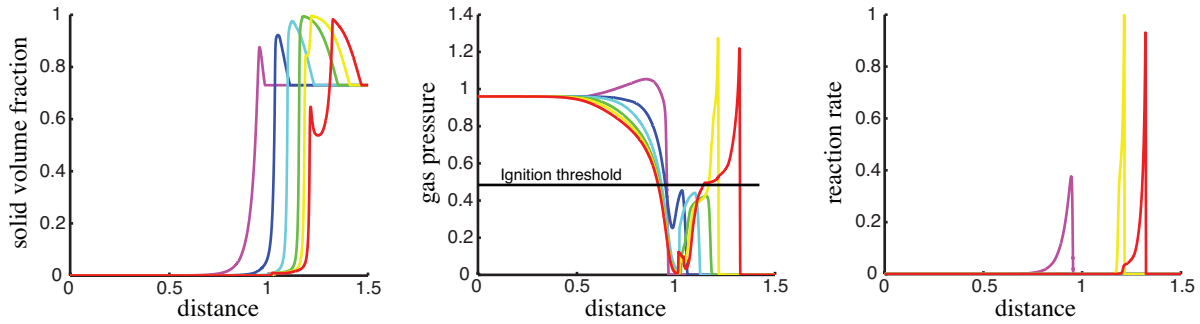

Figure 19: Case III ($\sigma = 25$, $p_{\text{ign}} = 0.48$): Profiles of solid volume fraction (left), gas pressure (middle) and reaction rate (right) along the wall at times $t = 1.0,\ 1.2,\ 1.4,\ 1.6,\ 1.7$ and 1.8.

Shaded contours for intermediate times $t = 2.0$ to 2.6 are shown in Figure 24. At $t = 2.0$ the lateral disturbance has undergone a reflection and is now traveling away from the wall. This disturbance, in the form of a gas shock at pressures above the ignition threshold, is traversing a region that contains some unreacted material. It therefore initiates reaction in which the said material is consumed. Meanwhile, as shown in the intermediate-time wall plots of Figure 25, the post-reflection evolution at the wall experiences a continual drop in the gas pressure, with an accompanying decline in the reaction rate. At $t = 2.6$ the reaction peak has fallen to 20% of its value at $t = 2.0$.

The strength of the wave continues to decline in the near-wall region. The shaded contour plots for times $t = 2.8$ to 4.0 in Figure 26 show the development and growth of a pocket of extinguished reaction, where the wave has degenerated into a compaction front. This feature is reinforced in the wall plots of Figure 27, which show the broadening compaction zone and the existence of sub-ignition values of the gas pressure downstream of the corner. Effectively, therefore, diffraction has given rise to a dead zone.

6 Conclusions

This paper presents the first diffraction study of the two-phase model of heterogeneous explosives. The intent has been to determine whether dead zones (pockets of extinguished reaction) are feasible within the model as postulated, or does one need to include additional complexity, in the reaction rate for example, to admit them. The study demonstrates that the pressure threshold for ignition and the reaction-rate prefactor can indeed act in concert to produce dead zones by themselves, without the introduction of additional mechanisms.

Diffraction past the corner creates a region of extinguished reaction in the vicinity of the corner, owing to a drop in the gas-phase pressure below the ignition threshold. The higher the ignition threshold, the larger the pocket of extinction created at this stage. The loss of reactive support weakens the gas-phase shock even more than the diffraction-induced expansion alone. Away from the corner the drop in the gas-phase pressure is less severe and the reaction continues, albeit at a reduced rate. The larger the reaction-rate prefactor, the stronger is the reaction in this region of reduced reaction rate. The reduction in rate causes the gas-phase shock to lose speed, but to a much lesser extent than in the near-wall region. A gradient of shock speed, and an associated gradient of post-shock gas-phase pressure, is therefore setup along the gas-phase shock. This gradient drives the reaction-supported segment of the gas-phase shock towards the wall, allowing it to overtake the unsupported segment of the shock there, and thereby raising the local gas-phase pressure. The larger the reaction-rate prefactor, the stronger is the gas-phase pressure rise. If the higher pressure overcomes the ignition threshold, then the reaction switches on again in a segment of the hitherto extinguished region behind the gas-phase shock and adjacent to the wall, whose extent is determined by the ignition threshold; the higher the ignition threshold, the thinner is the region in which the reaction is revived. As the wave advances along the wall, too thin a reaction zone may be unable to couple with the wave and the reaction may extinguish again, thereby resulting in a sustained dead zone of unreacted material. This is the scenario

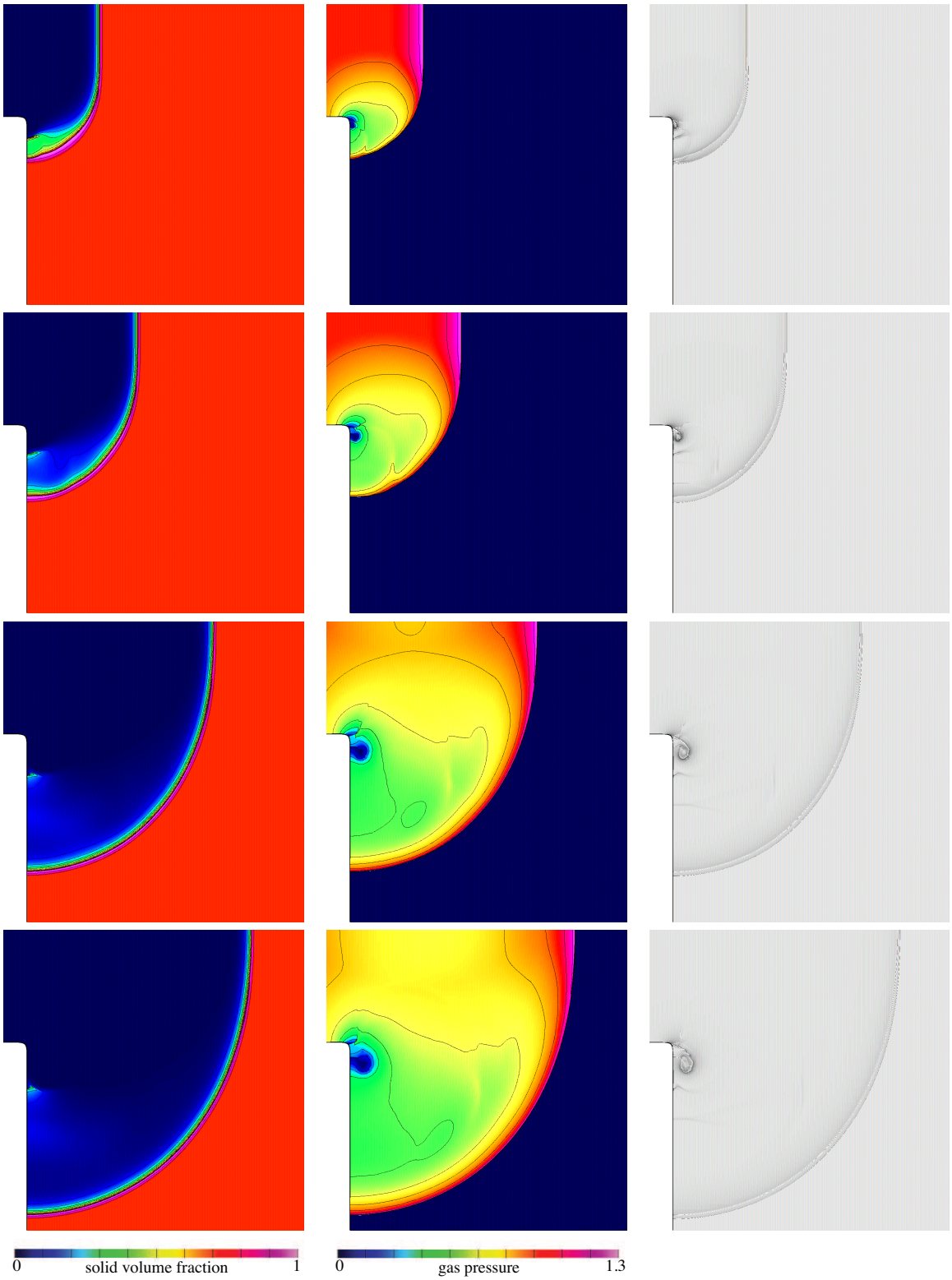

Figure 20: Case III ($\sigma = 25$, $p_{\text{ign}} = 0.48$): Shaded contours of solid volume fraction $\bar{\alpha}$ (left), gas pressure p (middle) and numerically generated schlieren (right) at times $t = 2.0$ (first row), $t = 2.5$ (second row), $t = 3.5$ (third row) and $t = 4.0$ (fourth row).

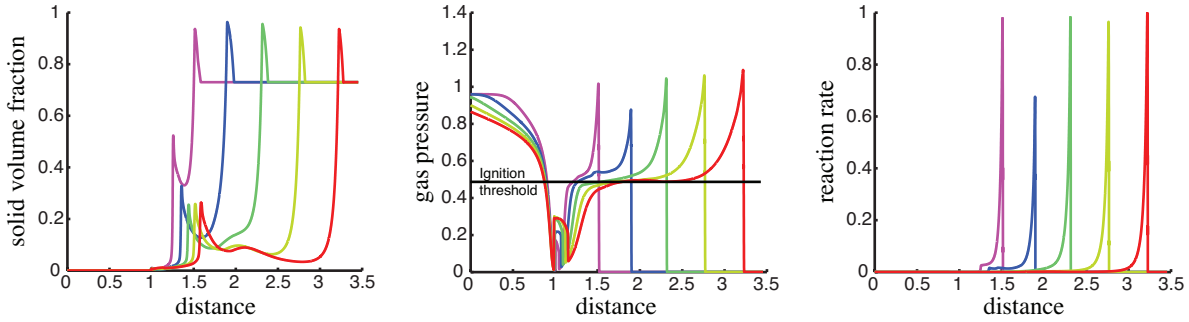

Figure 21: Case III ($\sigma = 25$, $p_{\text{ign}} = 0.48$): Profiles of solid volume fraction (left), gas pressure (middle) and the reaction rate (right) along the wall at times $t = 2.0, 2.5, \ldots, 4.0$

for Case IV, as seen in the late-time shaded contour plots of Figure 26 and in the mid-time and late-time wall plots of Figures 25 and 27 respectively. A somewhat thicker reaction zone will persist and result in a more-or-less quasisteady wave structure, in which a zone of high level of compaction is followed by a thin zone of reaction, which in turn is followed by a thicker zone of extinguished reaction but a lower level of compaction, i.e. a dead zone of partially reacted material. This state of affairs exists for Case II, as seen in the shaded contour plots of Figure 16 and the late-time wall plots of Figure 17. A still thicker reaction zone will couple with the gas-phase shock and coax the structure towards a fully fledged detonation, as happens in Case III and is shown in the shaded contour plots of Figure 20 and the late-time wall plots of Figure 21. Case I shows a similar inclination, but the amplification of the wave occurs much too slowly for it to mature before it runs out of room and exits the configuration; see Figure 12 and the late-time wall plots of Figure 13.

This behavior is at variance with what one finds in the ignition-and-growth model [12, 13]. There, pockets of extinguished reaction appear downstream of the corner and near the confining wall only for short times, and are overrun by strong lateral disturbances that originate in the interior of the domain, see Figure 18 in [13] for example. Sustained dead zones are admitted only in an enhanced ignition-and-growth model that takes into account the desensitization of the explosive due to the passage of weak shocks. The reason why the original ignition-and-growth model is unable to admit dead zones lies in the postulated form of the reaction-rate in that model, which employs a density threshold for ignition. Diffraction past the corner produces much smaller changes in density than in pressure, which accounts for the reduced sensitivity of the reaction rate to diffraction in the ignition-and-growth model. This also suggests why replacing a rigid confinement with a compliant confinement in that model does not promote the appearance of dead zones. We anticipate that compliant confinement of the two-phase model may aid further in producing dead zones, and are presently engaged in extending our numerical scheme to investigate that possibility. Higher values of ambient compaction are also under study.

7 Acknowledgements

Research support for DWS and AKK was provided by the National Science Foundation (NSF) under grant DMS-0609874. Additional support for DWS was given by Lawrence Livermore National Laboratory (LLNL) under subcontract B574692. The work of WDH was performed under the auspices of the U.S. Department of Energy (DOE) by LLNL under Contract DE-AC52-07NA27344 and with the support of the ASCR Applied Math Program of the DOE Office of Science. Numerical results were obtained using the Applied Math Cluster at RPI which was purchased in part using funds from the NSF grant DMS-0532160.

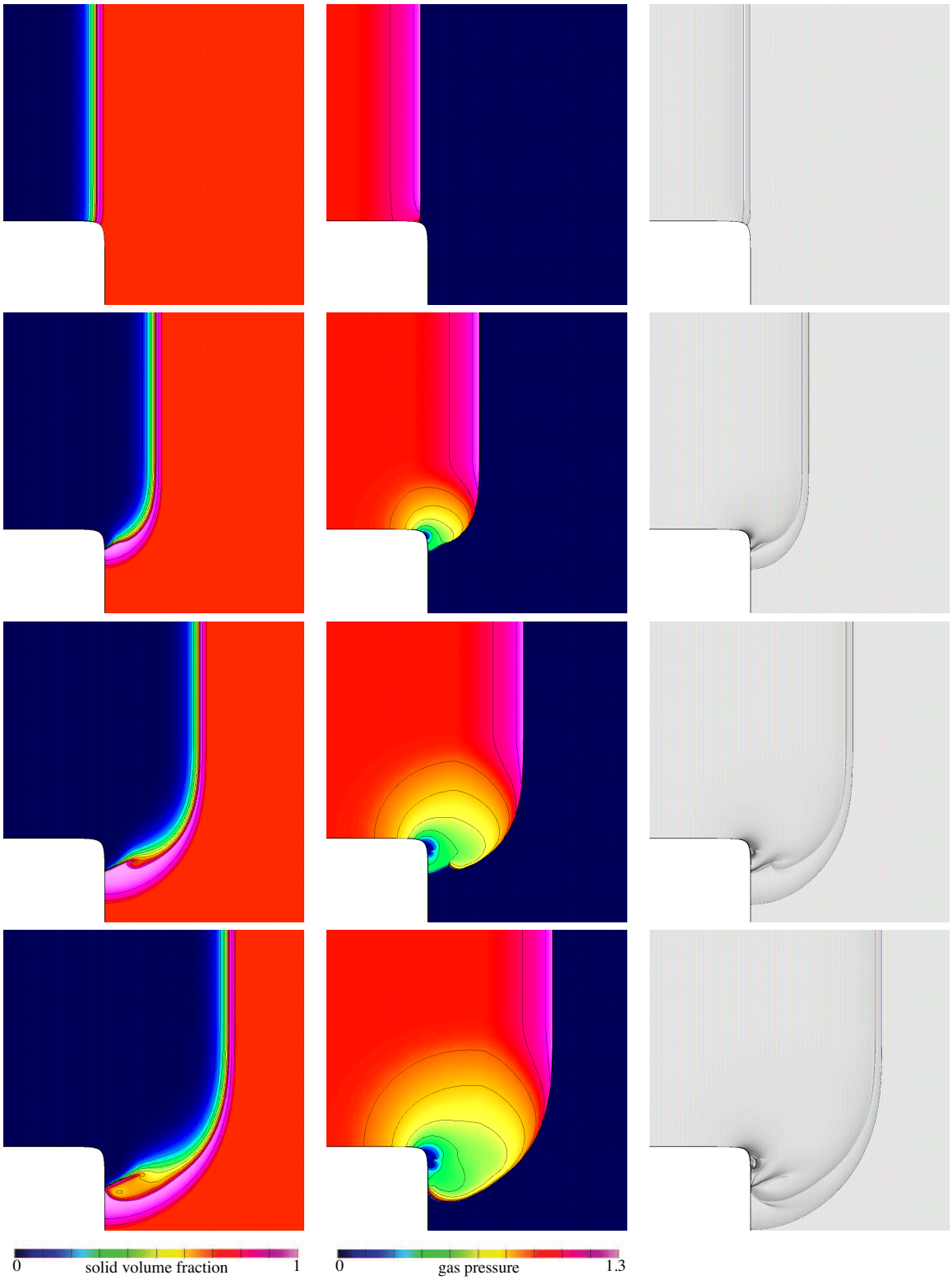

Figure 22: Case IV ($\sigma = 25$, $p_{\text{ign}} = 0.53$): Shaded contours of solid volume fraction $\bar{\alpha}$ (left), gas pressure p (middle) and numerically generated schlieren (right) at times $t = 1.0$ (first row), $t = 1.4$ (second row), $t = 1.7$ (third row) and $t = 1.9$ (fourth row).

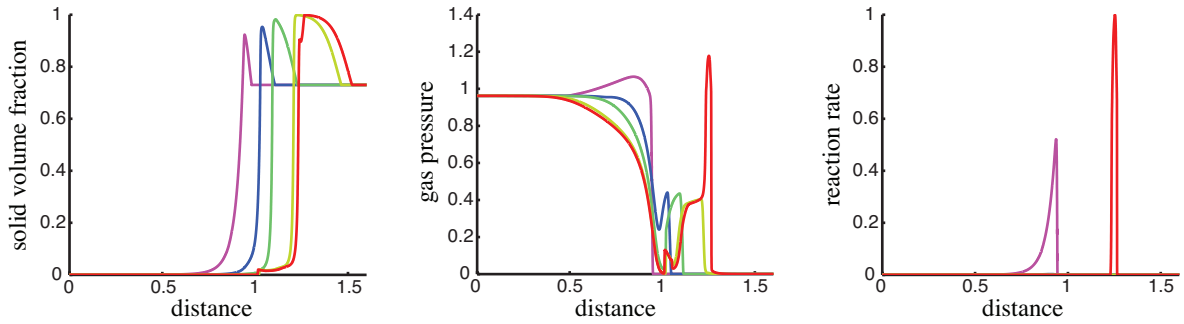

Figure 23: Case IV ($\sigma = 25$, $p_{\text{ign}} = 0.53$): Profiles of solid volume fraction (left), gas pressure (middle) and reaction rate (right) along the wall at times $t = 1.0, 1.2, \ldots, 1.8$ and 1.9 .

References

[1] E. L. Lee, C. M. Tarver, Phenomenological model of shock initiation in hetrogeneous explosives, Phys. Fluids 23 (12) (1980) 2362–2372.

[2] C. M. Tarver, J. O. Hallquist, L. M. Erickson, Modelling short-pulse duration shock initiation of solid explosives, in: The Eighth Symposium (International) on Detonation, 1985, pp. 951–960.

[3] C. M. Tarver, J. W. Kury, R. D. Breithaupt, Detonation waves in triaminonitrobenzene, J. Appl. Phys. 82 (1997) 3771–3782.

[4] J. W. Kury, R. D. Breithaupt, C. M. Tarver, Detonation waves in trinitrotoluene, Shock Waves 9 (1999) 227–237.

[5] C. M. Tarver, E. M. McGuire, Reactive flow modeling of the interaction of TATB detonation waves with inert materials, in: The Twelfth Symposium (International) on Detonation, 2002, pp. 641–649.

[6] M. R. Baer, J. W. Nunziato, A two-phase mixture theory for the deflagration-to-detonation transition (DDT) in reactive granular materials, Int. J. Multiphase Flow 12 (1986) 861–889.

[7] M. R. Baer, R. J. Gross, J. W. Nunziato, An experimental and theoretical study of deflagration-to-detonation transition (DDT) in the granular explosive CP, Combustion and Flame 65 (1986) 15–30.

[8] M. R. Baer, J. W. Nunziato, Compressive combustion of granular materials induced by low-velocity impact, in: The Ninth Symposium (International) on Detonation, 1989, pp. 293–305.

[9] E. Ferm, C. Morris, J. Quintana, P. Pazuchanic, H. Stacy, J. Zumbro, G. Hogan, N. King, Proton radiography examination of unburned regions in PBX 9502 corner turning experiments, Tech. Rep. LA-UR-01-3555, Los Alamos National Laboratory (2001).

[10] P. C. Souers, R. Garza, P. Vitello, Ignition and growth and JWL++ detonation models in course zones, Propellants, Explosives and Pyrotechnics 27 (2002) 62–71.

[11] C. M. Tarver, Ignition-and-growth modeling of LX-17 hockey puck experiments, Propellants, Explosives and Pyrotechnics 30 (2005) 109–117.

[12] A. K. Kapila, D. W. Schwendeman, J. B. Bdzil, W. D. Henshaw, A study of detonation diffraction in the ignition-and-growth model, Combust. Theory and Modeling 11 (2007) 781–822.

[13] J. B. Banks, D. W. Schwendeman, A. K. Kapila, W. D. Henshaw, A study of detonation propagation and diffraction with compliant confinement, Combust. Theory Modeling 12 (2008) 769–808.

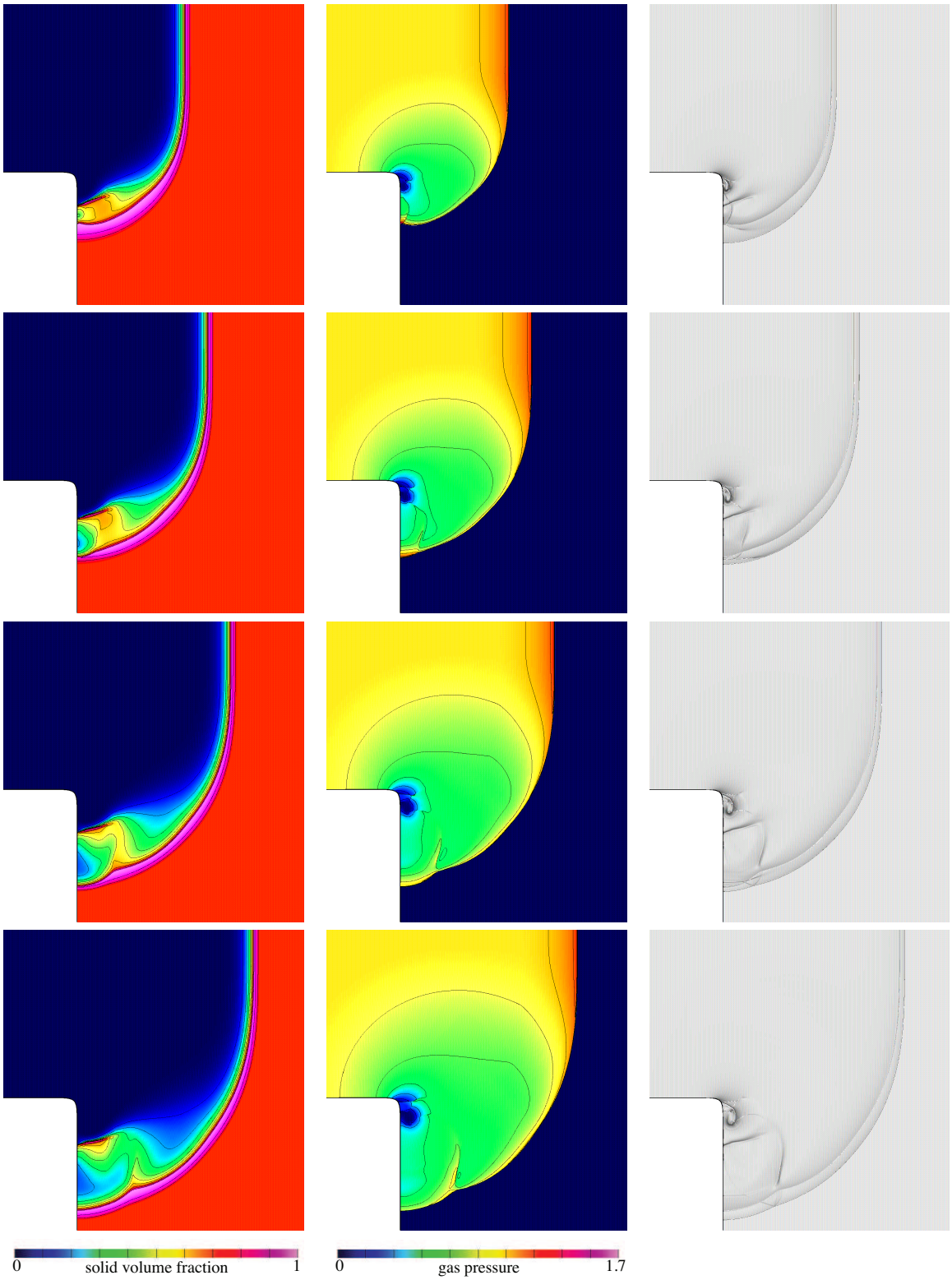

Figure 24: Case IV ($\sigma = 25$, $p_{\text{ign}} = 0.53$): Shaded contours of solid volume fraction $\bar{\alpha}$ (left), gas pressure p (middle) and numerically generated schlieren (right) at times $t = 2.0$ (first row), $t = 2.2$ (second row), $t = 2.4$ (third row) and $t = 2.6$ (fourth row).

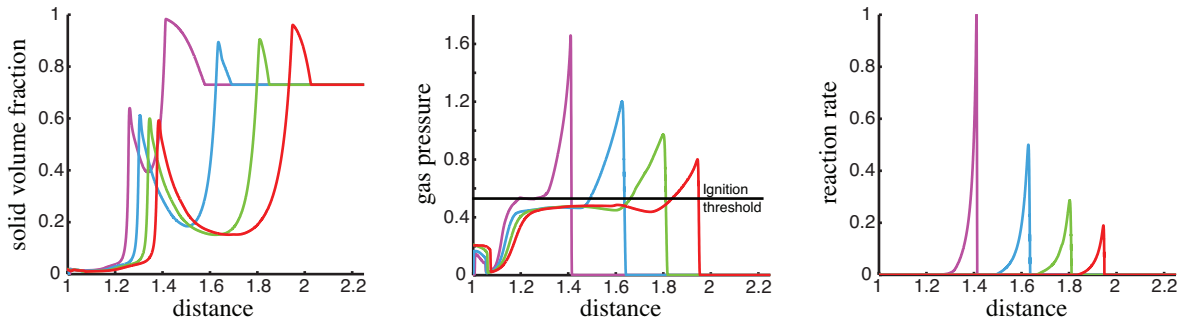

Figure 25: Case IV ($\sigma = 25$, $p_{\text{ign}} = 0.53$): Profiles of solid volume fraction (left), gas pressure (middle) and reaction rate (right) along the wall at times $t = 2.0,\ 2.2,\ 2.4,\ 2.6$.

[14] G. de Olivera, A. K. Kapila, D. W. Schwendeman, J. B. Bdzil, W. D. Henshaw, C. M. Tarver, Detonation diffraction, dead zones, and the ignition-and-growth model, in: The Thirteenth Symposium (International) on Detonation, 2006.

[15] B. L. Wescott, D. S. Stewart, W. C. Davis, Modeling diffraction and dead zones in PBX-9502, in: The Thirteenth Symposium (International) on Detonation, 2006.

[16] D. W. Schwendeman, C. W. Wahle, A. K. Kapila, The Riemann problem and a high-resolution Godunov method for a model of compressible two-phase flow, J. Comput. Phys. 212 (2006) 490–526.

[17] D. W. Schwendeman, C. W. Wahle, A. K. Kapila, A study of detonation evolution and structure for a model of compressible two-phase reactive flow, Combust. Theory and Modeling 12 (2008) 159–204.

[18] W. D. Henshaw, D. W. Schwendeman, An adaptive numerical scheme for high-speed reactive flow on overlapping grids, J. Comput. Phys. 191 (2) (2003) 420–447.

[19] W. D. Henshaw, D. W. Schwendeman, Parallel computation of three-dimensional flows using overlapping grids with adaptive mesh refinement, J. Comput. Phys. 227 (2008) 7469–7502.

[20] K. A. Gonthier, J. M. Powers, A numerical investigation of transient detonation in granulated material, Shock Waves 6 (1996) 183–195.

[21] K. A. Gonthier, J. M. Powers, A high-resolution numerical method for a two-phase model of deflagration-to-detonation transition, J. Comput. Phys. 163 (2000) 376–433.

[22] A. Chinnayya, E. Daniel, R. Saurel, Modelling detonation waves in heterogeneous energetic materials, J. Comput. Phys. 196 (2004) 490–538.

[23] J. B. Bdzil, R. Menikoff, S. F. Son, A. K. Kapila, D. S. Stewart, Two-phase modeling of deflagration-to-detonation transition in granular materials: A critical examination of modeling issues, Phys. Fluids 11 (2) (1999) 378–402.

[24] J. M. Powers, Two-phase viscous modeling of compaction in granular explosives, Phys. Fluids 16 (8) (2004) 2975–2990.

[25] M. J. Berger, J. Oliger, Adaptive mesh refinement for hyperbolic partial differential equations, J. Comp. Phys. 53 (1984) 484–512.

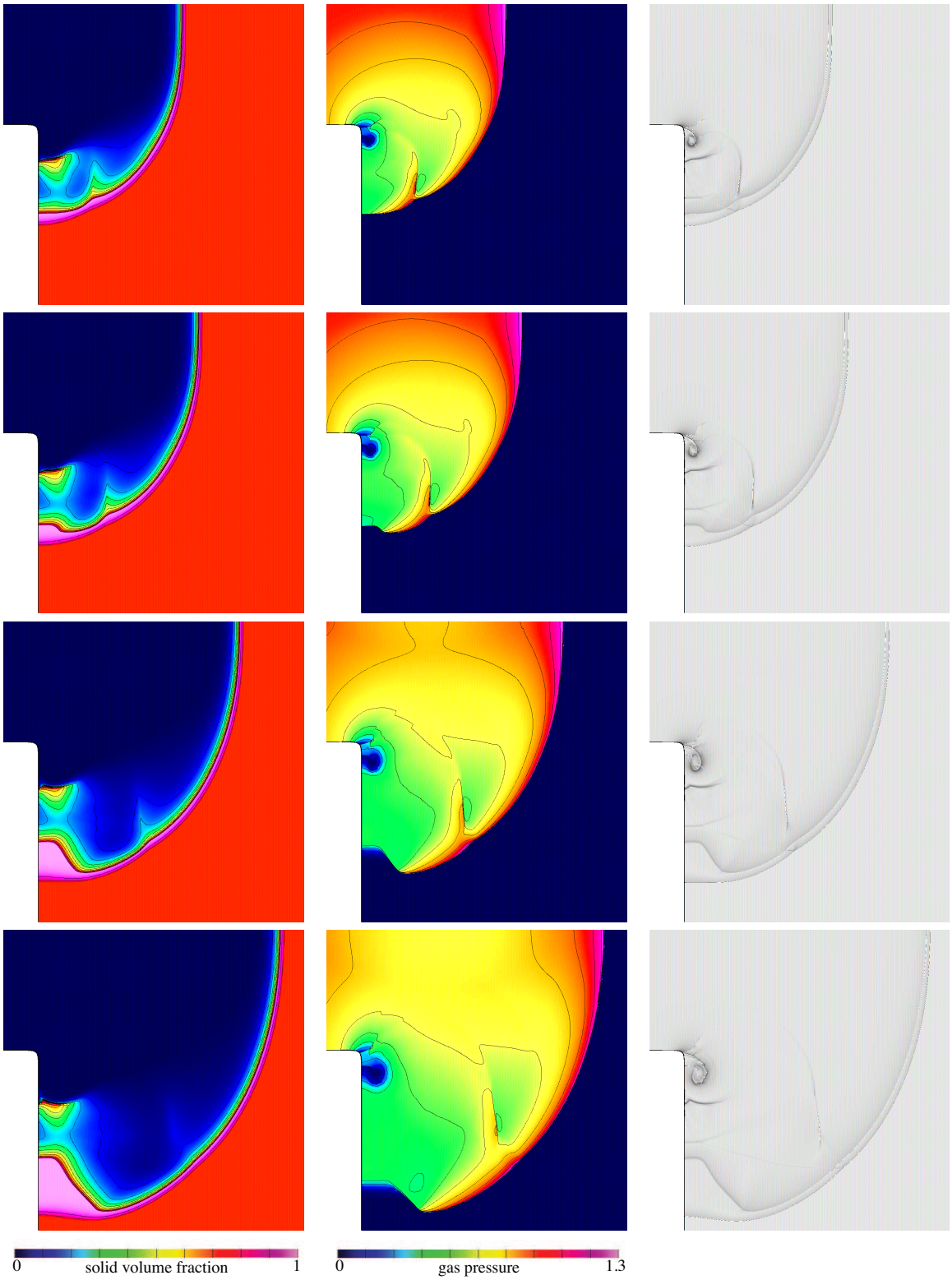

Figure 26: Case IV ($\sigma = 25$, $p_{\text{ign}} = 0.53$): Shaded contours of solid volume fraction $\bar{\alpha}$ (left), gas pressure p (middle) and numerically generated schlieren (right) at times $t = 2.8$ (first row), $t = 3.0$ (second row), $t = 3.5$ (third row) and $t = 4.0$ (fourth row).

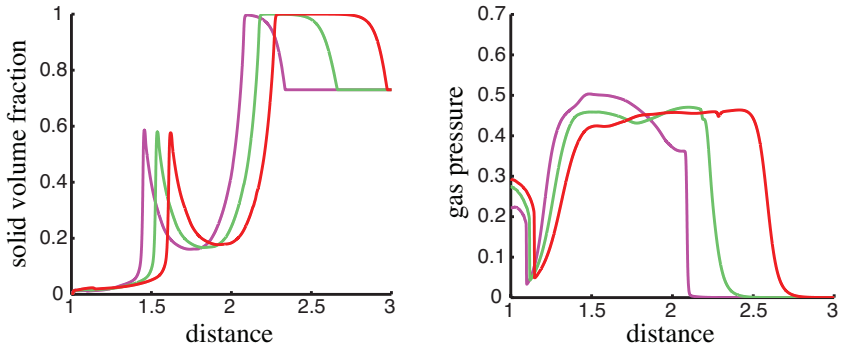

Figure 27: Case IV ($\sigma = 25$, $p_{\text{ign}} = 0.53$): Profiles of solid volume fraction (left) and gas pressure (right) along the wall at times $t = 3.0,\ 3.5,\ 4.0$.